**文部科学省 ［先端研究基盤共用・プラットフォーム形成事業 成果報告］**
兵庫県立大学 高度産業科学技術研究所 ニュースバル放射光施設

# レーザー逆コンプトンガンマ線を用いた光中性子断面積測定

| | | | |
|---|---|---|---|
| **所属** | 甲南大学理工学部 | **ビームライン** | BL01 |
| **利用者氏名** | 宇都宮　弘章 | **利用分野** | 量子ビーム技術 |
| **利用年度** | 2015年度 | **活用技術** | ガンマ線利用 |

## 利用成果の概要

209Bi(gamma,xn), (x=1−3) 断面積 データを7 – 40 MeVのエネルギー領域で取得した。ELI-NP研究所（ルーマニア）とモスクワ大学（ロシア）との共同研究として実施した。

7Li(gamma,n)断面積データを2 – 5 MeVのエネルギー領域で取得した。甲南大学理工学部物理学科卒業研究および自然科学研究科物理学専攻修士課程の研究として行った。

205Tl(gamma,n), 203Tl(gamma,n), 89Y(gamma,n)断面積データを7.7 – 20 MeVのエネルギー領域で取得した。9Be(gamma,xn), (x=1,2)断面積データを17 – 32 MeVのエネルギー領域で取得した。オスロ大学（ノルウェー）、ELI-NP（ルーマニア）との共同研究として実施した。レーザー逆コンプトンガンマ線の生成と診断は甲南大学理工学部物理学科卒業研究となる。また、9Be核データは自然科学研究科物理学専攻修士課程の学位取得の基になる。

## <利用目的>

次の光中性子断面積データを取得するためにレーザー逆コンプトンガンマ線を利用する。
1. 209Bi(gamma,xn), (x=1−3) 断面積 データ
2. 7Li(gamma,n)断面積データ
3. 205Tl(gamma,n), 203Tl(gamma,n), 89Y(gamma,n)断面積データ
4. 9Be(gamma,xn), (x=1,2)断面積データ

## <実験方法>

上記1, 4の(gamma,2n), (gamma,3n)核データを取得するために、レーザー逆コンプトンガンマ線をINAZUMA (Nd:YVO4)Q-switchレーザーの2倍高調波532nmを用いて生成した。電子エネルギーは630- 1100 MeVの範囲で変化させた。Pockels CellとPolarizerを用いてINAZUMAの周波数16.67 kHz（パルス間隔60ms）を1.04 kHz（パルス間隔960ms）に間引いた。中性子はエネルギー領域0 – 5 MeVで全検出効率が約40%の平坦効率中性子検出器で検出した。

上記2の(gamma,n)核データを取得するために、レーザー逆コンプトンガンマ線をCO2 CWレーザーの10.5915mmを用いて生成した。電子エネルギーは1020-1460 MeVまで変化させた。上記1, 3, 4の(gamma,n)核データを取得するために、レーザー逆コンプトンガンマ線をINAZUMA (Nd:YVO4)Q-switchレーザーの基本波1064nmを用いて生成した。電子エネルギーは651- 1061 MeVの範囲で変化させた。INAZUMAレーザーを20 kHzで動作させた。中性子は1MeV以下のエネルギー領域で60%以上の全検出効率を持つ高効率中性子検出器で検出した。

## <実験結果>

上記核データ1, 2, 3, ,4をそれぞれ取得することができた。現在、甲南大学、ELI-NP研究所、オスロ大学でそれぞれ分担してデータ解析を行っている。

## <今後の見通し>

上記核データ1と4は、国際研究プロジェクトIAEA-CRP F41032 Updating the photonuclear sata libraryに提供する。核データ3は国際研究プロジェクトIAEA-CRP F41032 Generating a reference dayabase for photon strength functionsに提供する。研究成果を基に、2016年9月11-16日にブルージュ（ベルギー）で開催される国際会議ND2016(International Conference on Nuclear Data for Science and Technology, http://www.nd2016.eu）で口頭発表3件、ポスター発表2件を予定している。

問い合わせ先
兵庫県立大学 高度産業科学技術研究所
ニュースバル放射光施設 共用促進室

〒678-1205 兵庫県赤穂郡上郡町光都1-1-2
TEL : 0791-58-2543　FAX : 0791-58-2504
E-mail : kyoyo@lasti.u-hyogo.ac.jp

ISSN 2189-0803

24aCE-1

# しきい値領域での $^9$Be の光核分解反応断面積の精密測定

甲南大理工、東大 CNS [A]、阪大 RCNP [B]、兵庫県立大 [C]、ELI-NP [D]
宇都宮弘章、片山誠太郎、河合義秋、今井奨、赤松勇樹、山口英斉 [A]、D. Kahl [A]、坂口裕司 [A]、嶋達志 [B]、高久圭二 [B]、宮本修治 [C]、山口将志 [C]、武元亮頼 [C]、I. Gheorghe [D]

ニュースバル放射光施設で高度に単色化されたレーザー逆コンプトンガンマ線ビームを用いて、中性子しきい値付近に存在する $^9$Be 核の $1/2^+$準位に対応する光中性子断面積を精密測定した。ターゲットには 25mm ϕ x 40mm, 99%の $^9$Be 棒を用いた。

$^9$Be の光分解反応断面積は、超新星爆発時の $^9$Be 核合成過程$\alpha\alpha \rightleftarrows {}^8\mathrm{Be}(n,\gamma){}^9\mathrm{Be}$ の逆反応断面積に相当する他、ポテンシャルバリアーのない s 波中性子がどのようにしてしきい値近傍に共鳴的な状態を作るかという原子核構造上の問題に関連する。

当該反応断面積は、これまで、放射性同位体の遷移ガンマ線や制動放射を使って測定された他、旧電総研でレーザー逆コンプトン（LCS）ガンマを用いて測定されている。最近デューク大学 HIGS 施設で LCS ガンマ線を使って行われた測定は、従来データと比べてピーク断面積で約 30%大きい反応断面積を報告している。

この反応断面積の測定は、ガンマ線ビームで$\alpha\alpha$n 3 体しきい値（1573 keV）と $^8$Be-n 2 体しきい値(1665 keV) を掃過する必要があるため、単色性に優れたガンマ線を利用することとガンマ線のエネルギー分布を定量的に理解することが不可欠となる。左図は今回の実験で使用した LCS ガンマ線に対する高純度 Ge 検出器の応答関数を示す。GEANT4 シミュレーションによって応答関数は見事に再現されている。これにより入射ガンマ線のエネルギースペクトルを精度よく決定することができた。右図は得られた反応断面積を HIGS データと比較したものである。反応断面積のしきい値近傍の振る舞いは HIGS から報告されたものとは大きく異なっている。

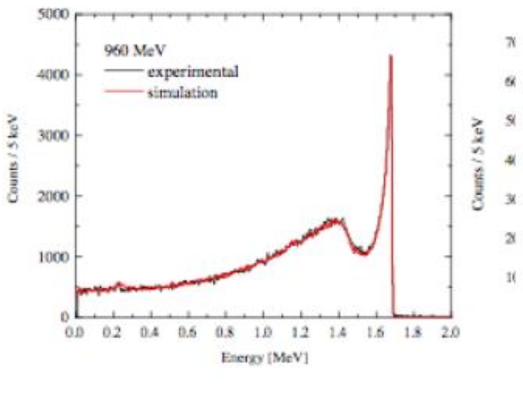

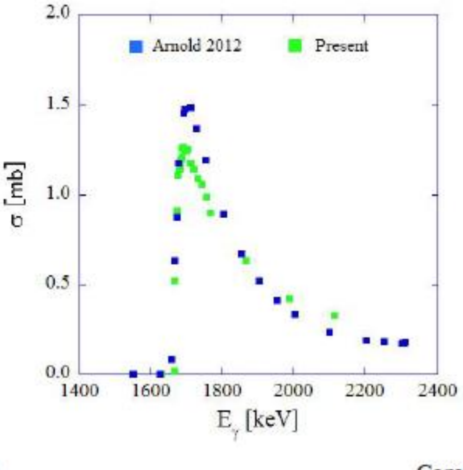

PHYSICAL REVIEW C **90**, 064616 (2014)

# Photoneutron cross sections for samarium isotopes: Toward a unified understanding of $(\gamma,n)$ and $(n,\gamma)$ reactions in the rare earth region

D. M. Filipescu,[1,2] I. Gheorghe,[1,2,3] H. Utsunomiya,[4,5] S. Goriely,[6] T. Renstrøm,[7] H.-T. Nyhus,[7] O. Tesileanu,[1] T. Glodariu,[2] T. Shima,[8] K. Takahisa,[8] S. Miyamoto,[9] Y.-W. Lui,[10] S. Hilaire,[11] S. Péru,[11] M. Martini,[6,11,12] and A. J. Koning[13]

[1]*Extreme Light Infrastructure Nuclear Physics, 407 Atomistilor Str., P.O. Box MG6, Bucharest-Magurele, Romania*
[2]*National Institute for Physics and Nuclear Engineering Horia Hulubei, 407 Atomistilor Str., P.O. Box MG6, Bucharest-Magurele, Romania*
[3]*Faculty of Physics, University of Bucharest, RO-077125, Bucharest, Romania*
[4]*Department of Physics, Konan University, Okamoto 8-9-1, Higashinada, Kobe 658-8501, Japan*
[5]*Center for Nuclear Study, University of Tokyo, 2-1 Hirosawa, Wako, Saitama 351-0198, Japan*
[6]*Institut d'Astronomie et d'Astrophysique, Université Libre de Bruxelles, Campus de la Plaine, CP-226, 1050 Brussels, Belgium*
[7]*Department of Physics, University of Oslo, N-0316 Oslo, Norway*
[8]*Research Center for Nuclear Physics, Osaka University, Suita, Osaka 567-0047, Japan*
[9]*Laboratory of Advanced Science and Technology for Industry, University of Hyogo, 3-1-2 Kouto, Kamigori, Ako-gun, Hyogo 678-1205, Japan*
[10]*Cyclotron Institute, Texas A&M University, College Station, Texas 77843, USA*
[11]*CEA, DAM, DIF, F-91297 Arpajon, France*
[12]*Department of Physics and Astronomy, Ghent University, Proeftuinstraat 86, B-9000 Gent, Belgium*
[13]*Nuclear Research and Consultancy Group, P.O. Box 25, NL-1755 ZG Petten, The Netherlands*

(Received 6 October 2014; revised manuscript received 24 November 2014; published 22 December 2014)

Photoneutron cross sections were measured for the seven stable samarium isotopes $^{144,147,148,149,150,152,154}$Sm near the neutron threshold with quasi-monochromatic laser-Compton scattering $\gamma$ rays. Our photoneutron cross sections are found to be low by 20%–37% relative to existing data. The photoneutron data are analyzed with the TALYS reaction code by considering the Skyrme Hartree-Fock-Bogoliubov (HFB) plus quasiparticle random phase approximation (QRPA) model and the axially symmetric deformed Gogny HFB plus QRPA model of the $E1$ $\gamma$-ray strength. Using the $\gamma$-ray strength function constrained by the present photoneutron data, we made a thorough analysis of the reverse $(n,\gamma)$ cross sections including the radioactive nucleus $^{151}$Sm with a half-life of 90 yr. The radiative neutron capture cross section for $^{153}$Sm with the half-life of 1.928 d is deduced with the $\gamma$-ray strength function method.

DOI: 10.1103/PhysRevC.90.064616 PACS number(s): 25.20.Lj, 25.40.Lw, 27.60.+j, 26.20.Kn

## I. INTRODUCTION

Radiative neutron capture on radioactive nuclei along the line of $\beta$ stability in the medium- to heavy-mass region of the chart of nuclei is an important issue in nuclear astrophysics and nuclear engineering. In nuclear astrophysics, the cross sections are important to determine the s-process path at branching points where neutron capture and $\beta$ decay compete [1]. The neutron capture data are also essential for nuclear transmutation of long-lived fission products known as nuclear waste in the field of nuclear engineering [2]. The $\gamma$-ray strength function ($\gamma$SF) method was recently devised for constraining the $(n,\gamma)$ cross section of radioactive nuclei, which cannot be measured directly [3,4]. This method relies on the Brink hypothesis linking photodeexcitation to photoabsorption [5] and aims at determining the $\gamma$SF, a nuclear statistical quantity that is commonly important to quantify radiative neutron capture and photoneutron cross sections. Photoneutron cross sections provide a stringent experimental constraint in absolute scale on the $\gamma$SF around the neutron emission threshold $S_n$. The method requires a systematic measurement of photoneutron cross sections for neighboring stable isotopes of a radioactive nucleus of interest, in addition to the existing $(n,\gamma)$ data which serve as experimental constraints on the $\gamma$SF below $S_n$. Thus, a unified understanding of $(n,\gamma)$ and $(\gamma,n)$ cross sections throughout an isotopic chain offers detailed information on the $\gamma$SF for a given nucleus formed by neutron capture on the radioactive nucleus. Such a systematic approach with the $\gamma$SF method has been applied to zirconium [6], tin [7], molybdenum [8], and neodymium [9] isotopes.

We now apply the $\gamma$SF method to the Sm isotopic chain. The $\gamma$SF method requires a systematic measurement of photoneutron cross sections for stable Sm isotopes in the vicinity of the radioactive Sm isotopes. Figure 1 illustrates the photoneutron emission and radiative neutron capture of Sm isotopes studied in the present paper. The present photoneutron measurement involved seven stable isotopes including the p-process nucleus $^{144}$Sm, the s-only nuclei $^{148}$Sm and $^{150}$Sm, and the r-only nucleus $^{154}$Sm as shown by the left-pointing arrows in Fig. 1. The photoneutron emissions studied constitute a part of the reaction network of the p-process nucleosynthesis [10] in which photodisintegration plays a primary role in reprocessing the preexisting nuclei produced by the s-process and r-process [11]. Photoneutron cross sections for two odd-$N$ nuclei, $^{147}$Sm and $^{149}$Sm, are measured for the first time. The $^{147}$Sm$(\gamma,n)$ reaction is important for the production of the p-process $^{146}$Sm chronometer [10]. The photodisintegration of $^{144}$Sm also contributes to the destruction of this p-process nucleus.

We present radiative neutron capture cross sections for $^{153}$Sm (half-life of 1.928 d) and $^{151}$Sm (half-life of 90 yr) determined with the $\gamma$SF method. The latter cross section

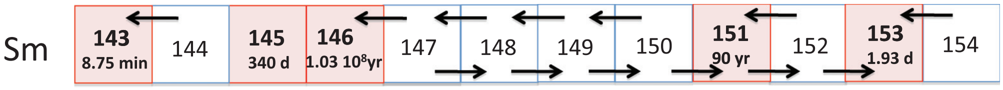

FIG. 1. (Color online) The chart of nuclei depicting our systematic analysis of $(\gamma,n)$ and $(n,\gamma)$ cross sections for Sm isotopes in the context of the $\gamma$-ray strength function method. Photoneutron cross sections measured in the present experiment are shown by left-pointing arrows. Radiative neutron capture cross sections discussed in the present systematic analysis are shown by right-pointing arrows. The radiative neutron capture cross section of the radioactive nucleus $^{153}$Sm is deduced with the $\gamma$-ray strength function method.

is compared with the direct measurement carried out at the CERN-nTOF facility [12,13].

The outline of the paper is given as follows: The experimental procedure is described in Sec. II, while details regarding the data analysis are given in Sec. III. The theoretical analysis for the photoneutron emission is described in Sec. IV. The radiative neutron capture cross sections, together with the determination of the $^{153}$Sm$(n,\gamma)^{154}$Sm cross section through the $\gamma$SF method, are analyzed in Sec. V . Finally, conclusions are drawn in Sec. VI.

## II. EXPERIMENTAL PROCEDURE

Photoneutron cross section measurements for the stable isotopes of samarium have been performed by using $\gamma$-ray beams produced by the Compton backscattering of laser photons on relativistic electrons (LCS $\gamma$ rays) at the NewSUBARU synchrotron radiation facility [14]. We present here details about $\gamma$ beam production, beam energy profile, target preparation, neutron detection, and beam flux monitoring.

### A. Gamma production and energy profile measurements

LCS $\gamma$-ray beams were produced with a high power $Q$-switch Nd : YVO$_4$ laser INAZUMA (Spectra-Physics) and electron beams at energies between 573 and 850 MeV. The maximum energy of the LCS $\gamma$-ray beams was varied from the corresponding neutron emission threshold ($S_n$) of each Sm isotope (the lowest value of which is 5.87 MeV for $^{149}$Sm) to 13 MeV, in the fundamental mode of the laser operation ($\lambda = 1064$ nm; power = 40 W). The laser was operated at a 20-kHz frequency and had a pulsed, 10-Hz macroscopic time structure of 80 ms beam-on and 20 ms beam-off. The electron beam intensity varied from 200 to 65 mA, decreasing by approximately 12–13 mA per hour.

The $\gamma$-ray beamline of the NewSUBARU synchrotron radiation facility is depicted in Fig. 2. The laser beam was focused in the vicinity of the midpoint (P2) of the straight section of the ring used for laser-electron interactions, where the electron beam has a minimum transverse profile and the probability of LCS interactions becomes maximum [14]. The LCS $\gamma$-ray beams were collimated with a 10-cm-thick lead block with a 2-mm opening (C2 collimator in Hutch 1) that is located 18.47 m from the interaction point. The collimator mounted on an $x$-$y$-$\theta$ stage driven by stepping motors was aligned to optimize the $\gamma$-ray flux by monitoring with a NaI(Tl) detector. The $\gamma$-ray beamline is equipped with a double collimation system with a 10-cm C1 lead collimator with 6- or 3-mm opening, which is located in the accelerator vault 3.00 m upstream from the C2 collimator. The experiment was carried out with and without the C1 collimator.

The $\gamma$-ray energy profile was measured with a large-volume 3.5″ × 4″ lanthanum bromide (LaBr$_3$ : Ce) detector in Hutch 2, GACKO (Gamma Collaboration Hutch of Konan University). Hourly measurements were performed for each $\gamma$-ray beam energy with the laser operated in the continuous-wave mode at a reduced power in order to avoid pile-up effects.

The LaBr$_3$ : Ce detector was calibrated by using the standard calibration sources $^{137}$Cs and $^{60}$Co including the 2.5-MeV sum peak of $^{60}$Co, the 1436-keV peak resulting from the electron capture decay of $^{138}$La, and the maximum energy of each LCS $\gamma$-ray beam produced in this experiment. The energy calibration of the LaBr$_3$ : Ce detector is shown in Fig. 3. The calibration points were fitted with a second-order polynomial by using the $\chi^2$ method. The energy resolution of the detector was studied by using $\gamma$ transitions from the $^{137}$Cs and $^{60}$Co sources. An upper limit of 2% was obtained for energies above 2.5 MeV by fitting the data points with a $1/\sqrt{E}$ function, where $E$ is the $\gamma$-ray energy.

The maximum energy of the LCS $\gamma$-ray beams is obtained by the known energy of the electrons and laser photons (1.164 eV). The electron beam energy was recently calibrated between 550 and 974 MeV in nominal energy with an accuracy of the order of $10^{-5}$ [15]. For this, a grating-fixed CO$_2$ laser ($\lambda = 10.5915$ $\mu$m) was used to produce low-energy LCS $\gamma$-ray beams below 1.7 MeV at the interaction point P1. The produced $\gamma$-ray beams were measured with a calibrated hyperpure Germanium (HPGe) detector. It was found that there

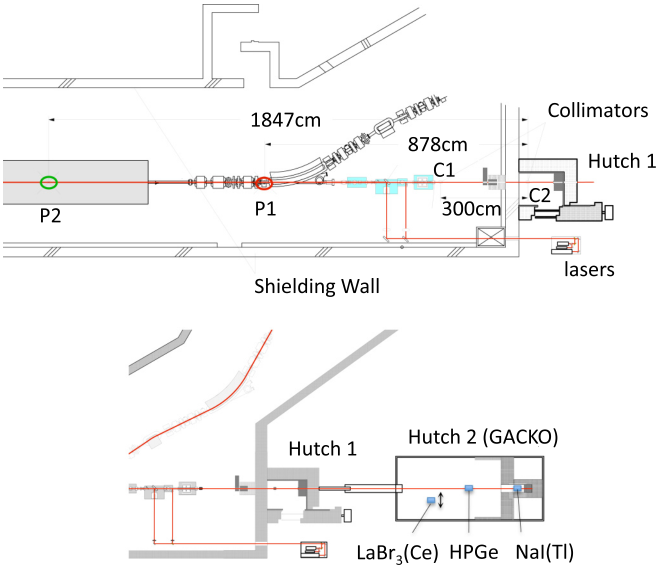

FIG. 2. (Color online) The $\gamma$-ray beamline at the NewSUBARU synchrotorn radiation facility.

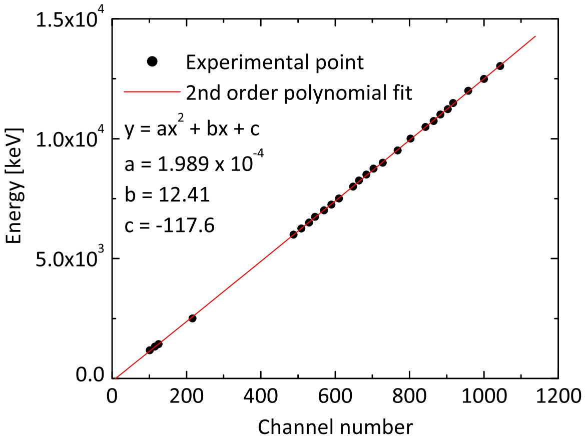

FIG. 3. (Color online) Energy calibration of the $\text{LaBr}_3:\text{Ce}$ detector with $^{137}$Cs, $^{60}$Co, and $^{138}$La and the maximum energies of LCS $\gamma$-ray beams produced using a Nd : $\text{YVO}_4$ laser and electron beams at energies between 573 and 850 MeV.

is a systematic difference of approximately 10 MeV between the nominal electron energy given by the beam optics of the storage ring and the calibrated energy.

The Compton backscattering of laser photons on relativistic electrons and the electromagnetic interactions of the $\gamma$-ray beams inside the $\text{LaBr}_3:\text{Ce}$ detector were simulated by using the GEANT4 Monte Carlo code [16,17]. The kinematics of the inverse Compton scattering is implemented in the Monte Carlo code with inclusion of the effect of the electron beam emittance. The energy spectra of the LCS $\gamma$-ray beams incident on the targets were obtained by reproducing the $\text{LaBr}_3:\text{Ce}$ detector response. A detailed description of the GEANT4 simulation is given in a separate paper [18].

Figure 4 shows a typical spectrum of the LCS $\gamma$-ray beam recorded with the $\text{LaBr}_3:\text{Ce}$ detector (solid line) along with the GEANT4 simulations of the detector response function (dotted line) and the incident $\gamma$-ray beam (gray line). The spectra are renormalized for better visualization. The experimental response function was obtained without the C1 collimator. One can see a broad low-energy bump around 3 MeV in the response function. This bump is characteristic of spectra obtained without the C1 collimator, which was confirmed experimentally under the presence and absence of the C1 collimator. The bump corresponds to the laser photons Compton-scattered around 0° with large cross sections in the rest frame of electrons which, after a Lorentz boost by relativistic electrons in the laboratory frame, punched through the 10-cm C2 collimator. The punch-through component is seen in the low-energy region of the incident $\gamma$-ray spectrum.

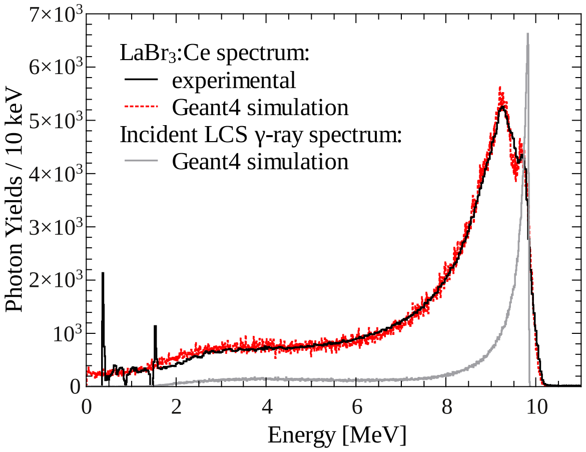

FIG. 4. (Color online) A typical spectrum of the $\gamma$-ray beam recorded with the $\text{LaBr}_3:\text{Ce}$ detector (solid line) and the simulations of the response function (dotted line) and of the incident $\gamma$-ray beam (gray line). A single collimation with a C2 collimator of 2-mm aperture was used.

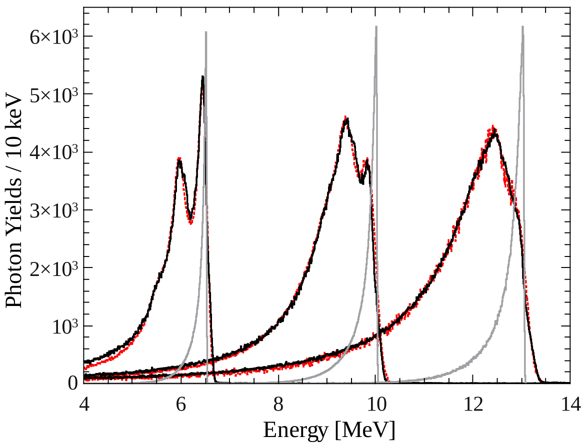

FIG. 5. (Color online) Typical spectra of the $\gamma$-ray beams recorded with the $\text{LaBr}_3:\text{Ce}$ detector (solid lines) and the simulations of the response function (dotted lines) and of the incident $\gamma$-ray beam (gray lines). A double collimation with a C1 collimator of 6-mm aperture and a C2 collimator of 2-mm aperture was employed.

Figure 5 shows typical spectra of the LCS $\gamma$-ray beams recorded with the $\text{LaBr}_3:\text{Ce}$ detector (solid lines) along with the GEANT4 simulations of the detector response function (dotted lines) and the incident $\gamma$-ray beam (gray lines). The experimental response functions were obtained by using the double collimation system with a C1 collimator of 6-mm aperture. The low-energy component is absent in the response function obtained with the double collimation system, which confines the scattering angles into a narrower cone along the electron beam axis with a total thickness of 20 cm. The experimental response functions are well reproduced by the GEANT4 simulation. Energy spreads of 1.2%, 1.4%, and 1.6% at full width at half maximum (FWHM) were obtained for the three incident $\gamma$-ray beams of maximum energy of 6.5, 10.0, and 13.0 MeV, respectively. Thus the $\text{LaBr}_3:\text{Ce}$ detector is suitable for recording energy spectra of the $\gamma$-ray beams.

### B. Target preparation

Enriched samples of $^{144}$Sm, $^{147}$Sm, $^{148}$Sm, $^{149}$Sm, $^{150}$Sm, $^{152}$Sm, and $^{154}$Sm in oxide form ($\text{Sm}_2\text{O}_3$) placed in pure aluminum containers with inner diameter of 8 mm were irradiated by the $\gamma$-ray beams. The samples were dehydrated by baking in vacuum at temperatures up to 393°C for 4 h before

TABLE I. Enrichment and areal density of samples.

| Sample | Purity (%) | Areal density (mg/cm$^2$) |
|---|---|---|
| $^{144}$Sm | 88.80 | 1102 |
| $^{147}$Sm | 94.00 | 1042 |
| $^{148}$Sm | 99.94 | 2102 |
| $^{149}$Sm | 97.72 | 2242 |
| $^{150}$Sm | 94.68 | 862 |
| $^{152}$Sm | 99.47 | 1959 |
| $^{154}$Sm | 98.69 | 2253 |

being placed inside the aluminum containers. The sample masses were determined by weighing the containers before and after the filling. The $\gamma$-ray beam was positioned at the center of the target by monitoring the visible synchrotron radiation as a guide. According to the GEANT4 simulation, the beam spot on target is 2.3 mm in diameter, which is sufficiently smaller than the diameter of the target. The enrichment and the areal density of each sample are listed in Table I.

### C. Neutron detection

The number of $(\gamma,n)$ reactions was determined by detecting the reaction neutrons with a calibrated neutron detection array. The samarium samples were mounted at the center of a $4\pi$ neutron detector composed of 20 $^3$He proportional counters embedded in a $36 \times 36 \times 50$ cm$^3$ polyethylene moderator. The $^3$He counters were placed in three concentric rings of four, eight, and eight proportional counters located 3.8, 7.0, and 10.0 cm from the beam axis, respectively. The moderator was surrounded by additional polyethylene plates with cadmium to suppress background neutrons. Every 100 ms of $\gamma$ irradiation, reaction plus background neutrons were recorded for 80 ms of laser-on and background neutrons were recorded for 20 ms of laser-off. The average energy of the reaction neutrons was obtained using the "ring ratio technique" originally developed by Berman and Fultz [19] and used to determine the detection efficiency. More details of the neutron detection are found in the literature [20].

Neutron detection efficiencies of the three rings were measured after the present experiment by using a calibrated $^{252}$Cf source with an emission rate of $2.27 \times 10^4$ s$^{-1}$ with 2.2% uncertainty at the National Metrology Institute of Japan. The measurement excellently reproduced the results obtained in 2006 at the same institute, which can be seen in Ref. [20].

### D. Beam flux monitoring

The $\gamma$-ray beam flux was monitored with a $6'' \times 5''$ NaI(Tl) detector placed at the end of the LCS $\gamma$-ray beam line. The Nd : YVO$_4$ ($\lambda = 1.064$ $\mu$m) laser operated at 20-kHz frequency produces pulses of light of 60 ns in duration. The electron beam bunches have a time structure of 2-ns interval (500 MHz) and 60-ps width. Thus, the LCS $\gamma$ rays are generated in bunches corresponding to each laser light pulse. The number of LCS $\gamma$ rays per bunch is given by a Poisson distribution [21] with a mean which depends on the laser and electron beam intensity, collimator aperture, and the probability of interaction between the laser photons and the relativistic electrons.

The number of recorded $\gamma$ photons was obtained by using the "pile-up method" described in [21], which is based on the Poisson fitting method originally developed at the Electrotechnical Laboratory [22,23]. The uncertainty of the Poisson fitting method is estimated to be 3%, which is attributed to the fitting and the energy linearity of the $\gamma$-ray detector in its response to multiphotons. For each neutron measurement run we recorded the $\gamma$-ray spectra, when the laser is on in the full power mode. Multiple photons were detected simultaneously, generating a so-called pile-up spectrum. Before or after each neutron measurement run the laser power is reduced in order to obtain a single-photon spectrum, where it is most likely to measure only one photon at a time. A typical example of the experimental pile-up energy spectrum, along with the single-photon spectrum, is shown in Fig. 6.

The number of $\gamma$ rays detected in the NaI detector, $N_{\gamma,\mathrm{det}}$, is given by

$$N_{\gamma,\mathrm{det}} = \frac{\langle i\rangle_{\mathrm{pileup}}}{\langle i\rangle_{\mathrm{single}}}\left(\sum n_i\right)_{\mathrm{pileup}}, \tag{1}$$

where $\langle i\rangle = (\sum x_i n_i)/(\sum n_i)$ gives the average channel of the pile-up and single-photon spectrum, and $n_i$ is the number of counts in the $i$th channel. Note that the ratio of $\langle i\rangle$ in Eq. (1) gives the average number of $\gamma$ photons involved in a $\gamma$-ray beam pulse, while the sum pile-up events give the number of $\gamma$-ray beam pulses. As the targets are quite thick, the attenuation of the $\gamma$ rays in the target amounts to 2%–3%. Furthermore, to calculate the average $\gamma$-ray flux incident on the target we have to take into account the attenuation in the NaI detector as well,

$$N_\gamma = \frac{N_{\gamma,\mathrm{det}}}{\exp\left[-\frac{\mu_t}{\rho_t}t_t\right]\left(1-\exp\left[-\frac{\mu_{\mathrm{NaI}}}{\rho_{\mathrm{NaI}}}t_{\mathrm{NaI}}\right]\right)}, \tag{2}$$

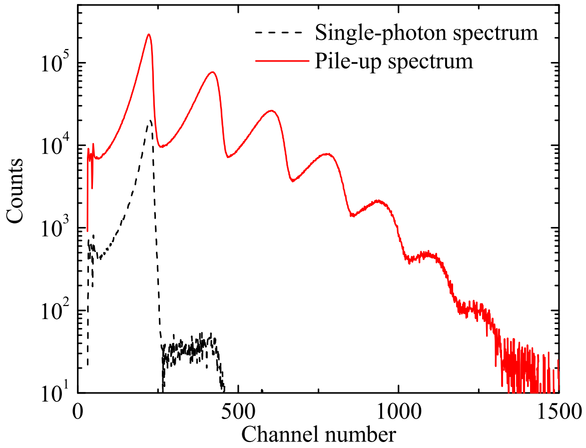

FIG. 6. (Color online) Experimental pile-up energy spectrum of the LCS $\gamma$-ray beam obtained with a $6'' \times 5''$ NaI(Tl) detector. A single-photon spectrum is also shown by the dashed line. The maximum energy of the LCS $\gamma$-ray beam is 13.03 MeV (electron beam energy of 860.8 MeV). The average number of photons per beam pulse is 1.78.

where $t_t$ and $t_{\rm NaI}$ give the thickness (in g/cm$^2$) of the target and the NaI detector, respectively, and $\frac{\mu}{\rho}$ represents the mass attenuation coefficient (in cm$^2$/g), tabulated in Ref. [24].

The systematic uncertainty for the cross section breaks down to 3% for the number of incident photons, 3.2% for the neutron detection efficiency, 0.5%–0.7% for the number of target nuclei, and 0.2%–0.9% for the total attenuation coefficient. Thus, the overall systematic uncertainty amounts to 4.5% by summing the uncertainties of the breakdown in quadrature.

## III. DATA REDUCTION

The photoneutron cross section is given by

$$\int_{S_n}^{E_{\rm Max}} n_\gamma(E_\gamma)\sigma_{\gamma n}(E_\gamma)dE_\gamma = \frac{N_n}{N_t N_\gamma \xi \epsilon_n g}, \tag{3}$$

where $n_\gamma(E_\gamma)$ gives the energy distribution of the $\gamma$-ray beam normalized to unity and $\sigma_{\gamma n}(E_\gamma)$ is the photoneutron cross section to be determined. Furthermore, $N_n$ represents the number of neutrons detected, $N_t$ gives the number of target nuclei per unit area, $N_\gamma$ is the number of $\gamma$ rays incident on target, $\epsilon_n$ represents the neutron detection efficiency, and finally $\xi = (1 - e^{\mu t})/(\mu t)$ gives a correction factor for a thick target measurement. The factor $g$ represents the fraction of $\gamma$ flux above the neutron threshold $S_n$,

$$g = \frac{\int_{S_n}^{E_{\rm Max}} n_\gamma(E_\gamma)dE_\gamma}{\int_{0}^{E_{\rm Max}} n_\gamma(E_\gamma)dE_\gamma}. \tag{4}$$

As a first approximation we assume a monochromatic $\gamma$-ray beam, by replacing the $\gamma$-energy distribution $n(E_\gamma)$ in Eq. (3) by a delta function, $\delta(E_\gamma - E_{\rm av})$. Here, $E_{\rm av}$ is the average energy of the LCS $\gamma$ beam,

$$E_{\rm av} = \frac{\int_{S_n}^{E_{\rm Max}} E_\gamma n_\gamma(E_\gamma)dE_\gamma}{\int_{S_n}^{E_{\rm Max}} n_\gamma(E_\gamma)dE_\gamma}. \tag{5}$$

We obtain the following cross section in the monochromatic approximation:

$$\sigma_{\gamma n}^{\rm mono}(E_{\rm av}) = \frac{N_n}{N_t N_\gamma \xi \epsilon_n g}. \tag{6}$$

The next step is to take into account the measured energy distribution of the $\gamma$-ray beam. A Taylor expansion method [25] is used to solve the integral of Eq. (3) with respect to $\sigma_{\gamma n}(E_{\rm av})$ in the following manner:

$$\sigma_{\gamma n}(E_{\rm av}) + \sum_i s_i(E_{\rm av}) = \frac{N_n}{N_t N_\gamma \xi \epsilon_n g}, \tag{7}$$

where

$$s_i(E_{\rm av}) = \frac{1}{n!}\sigma_{\gamma n}^{(i)}(E_{\rm av}) \int_{S_n}^{E_{Max}} n_\gamma(E_\gamma)(E_\gamma - E_{\rm av})^i dE_\gamma, \tag{8}$$

and where $\sigma_{\gamma n}^{(i)}(E_{\rm av})$ represents the $i$th derivative of $\sigma_{\gamma n}(E_{\rm av})$. In order to determine $\sigma_{\gamma n}^{(i)}(E_{av})$, one must assume an energy dependence; hence an iteration procedure must be applied. The iteration procedure consists of the following four steps:

1. We use the monochromatic cross section found from Eq. (6), $\sigma^{(0)}(E_{\rm av}) = \sigma_{\gamma n}^{\rm mono}(E_{\rm av})$, as our starting point and fit it with a Lorentzian function multiplied by a power law which dominates near $S_n$ energies,

   $$\sigma(E) = \sigma_c\left(\frac{E - S_n}{S_n}\right)^p \frac{1}{1 + \left(E^2 - E_R^2\right)^2/(E^2\Gamma^2)}, \tag{9}$$

   where $\sigma_c$, $p$, $E_R$, and $\Gamma$ are treated as free parameters [20].
2. The fitted function $\sigma(E)$ is further divided into small regions of 300 keV, and each region is fitted by a third-order polynomial.
3. The third-order polynomials are in turn used to calculate the derivatives $\sigma_{\gamma n}^{(i)}(E_{\rm av})$ in Eq. (8).
4. Combining Eqs. (6) and (7), we get $\sigma(E_{\rm av})$ by

   $$\sigma_{\gamma n}^{(1)}(E_{\rm av}) = \sigma_{\gamma n}^{\rm mono}(E_{\rm av}) - s_2(E_{\rm av}) - s_3(E_{\rm av}). \tag{10}$$

   Here, we notice that the $s_1$ term cancels out.
   The calculated photoneutron cross section $\sigma_{\gamma n}^{(1)}(E_{\rm av})$ is used for the next iteration; this procedure is followed until convergence is achieved.

We find that the series converges rather fast. Since the energy distribution of the beam is very sharp, the overall correction remains small, i.e., 0.5%–9%. As shown in Fig. 7, only cross sections located at the highest average energies are subject to a significant correction.

Our final photoneutron cross sections are compared in Figs. 8–14 with previous measurements, including the Saclay data [26]. Significant discrepancies are observed between our cross sections and those of Saclay for all Sm isotopes. Our experiment leads to cross sections lower by 20%–37%. Such an overestimate by the Saclay photodata was also reported in previous comparisons for $^{142}$Nd with a renormalization by a factor of 0.86 [31], for $^{144}$Sm by a factor of 0.80 [32], and for

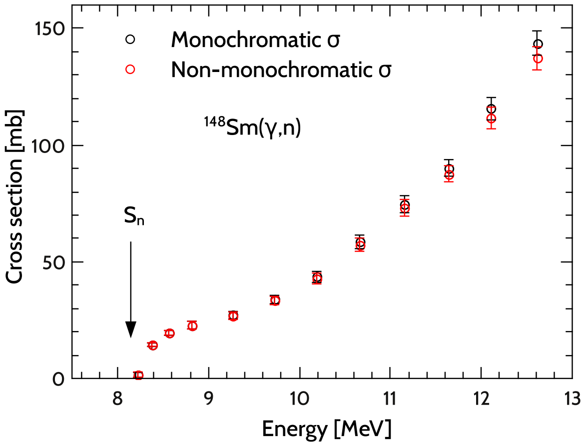

FIG. 7. (Color online) The monochromatic cross section and the nonmonochromatic cross section of $^{148}$Sm. The arrow-indicated $S_n$ gives the neutron threshold of this nucleus.

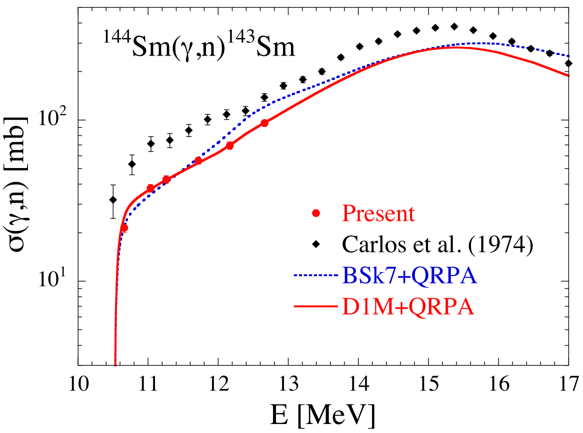

FIG. 8. (Color online) Comparison between the present photoneutron emission cross sections and previously measured ones [26] for $^{144}$Sm. Also included are the predictions from Skyrme HFB+QRPA (based on the BSk7 interaction) [27] and axially deformed Gogny HFB+QRPA models (based on the D1M interaction) [28].

$^{nat}$Rb, $^{nat}$Sr, $^{89}$Y, $^{90}$Zr, $^{93}$Nb, $^{127}$I, $^{197}$Au, and $^{208}$Pb by a factor of 0.80–0.93 [33].

## IV. THEORETICAL ANALYSIS

The photoneutron cross-section data are now compared with theoretical calculations obtained with the TALYS nuclear reaction code [34,35] and two different models of the $\gamma$SF, namely, the Skyrme Hartree-Fock-Bogoliubov (HFB) plus quasiparticle random phase approximation (QRPA) model [27] based on the BSk7 interaction and the axially symmetric deformed Gogny HFB plus QRPA model based on the D1M interaction [28,36–38]. Both models are based on the QRPA approach but make use of different interactions and approximations. The BSk7+QRPA model introduces some phenomenological corrections to take the damping of the collective motion as well as the deformation effects into account. In contrast, the D1M+QRPA model allows for a consistent description of axially symmetric deformations and includes phenomenologically the impact of multiparticle-multihole configuration as a function of their densities [28,37]. Both models have proven their capacity to reproduce experimental photoabsorption data relatively well.

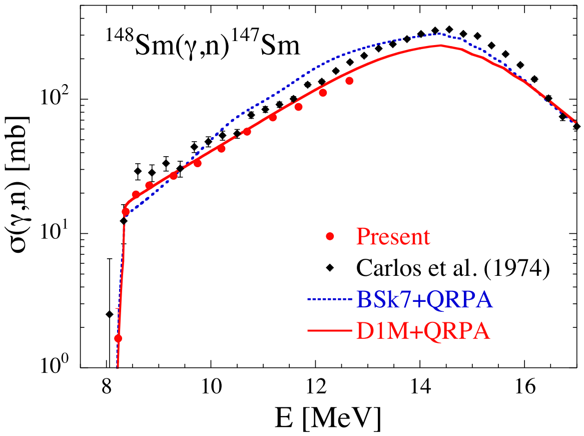

FIG. 10. (Color online) Same as Fig. 8 for $^{148}$Sm.

As seen in Figs. 8–14, cross sections around the neutron threshold are rather well described by the D1M+QRPA model, provided a scaling within typically 10%–20% is applied to the strength function to reproduce the absolute experimental cross sections. The agreement around the neutron threshold is rather satisfactory and there is no reason to invoke the presence of extra low-lying strength from the present data, at least in the vicinity of the neutron threshold and as seen in some previous photodata [3,6,7,39]. In contrast, larger deviations are seen for the predictions obtained with the BSk7+QRPA strength where some extra strength is usually predicted around 11 MeV. Similar quantitative and qualitative results were obtained in the analysis of the photoneutron data for the Nd isotopes [9].

## V. RADIATIVE NEUTRON CAPTURE AND THE $\gamma$SF METHOD

We now turn to the reverse radiative neutron capture channel. It should be kept in mind that the corresponding

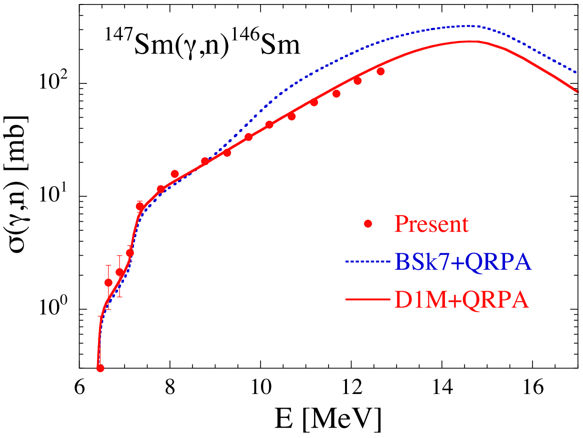

FIG. 9. (Color online) Same as Fig. 8 for $^{147}$Sm.

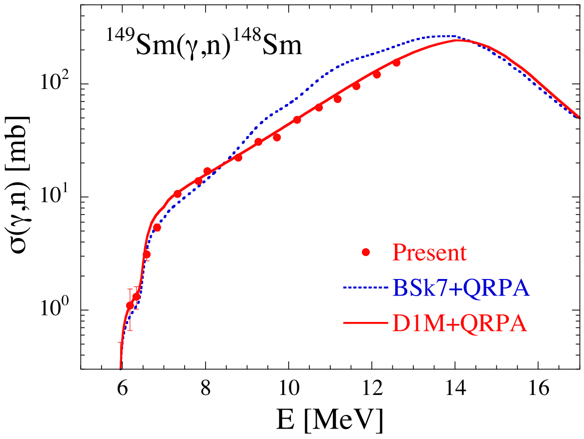

FIG. 11. (Color online) Same as Fig. 8 for $^{149}$Sm.

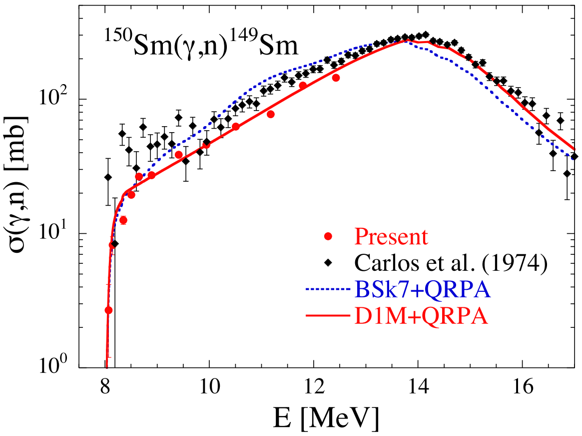

FIG. 12. (Color online) Same as Fig. 8 for $^{150}$Sm.

cross section for incident keV neutrons depends sensitively on the $\gamma$SF, but in a rather lower energy range below the neutron threshold, typically around 6 MeV of $\gamma$-ray energy for the stable Sm isotopes, corresponding to the major contributing energy range in the folding of the $\gamma$SF with the nuclear level density (NLD) [11,27]. The predicted tail of the strength function at low energies therefore plays a fundamental role.

On the basis of the Gogny HFB plus QRPA $\gamma$-ray strength [28], the reverse radiative neutron capture cross sections are now estimated with the TALYS reaction code [34,35] for the stable and experimentally known $^{147,148,149,150,151,152}$Sm isotopes and compared with the experimental cross sections [26,29,30] in Fig. 15. Note that, in addition to the $E1$ contribution to the $\gamma$SF, the smaller $M1$ and other higher multipolarities are included, following the prescriptions recommended in Refs. [34,35,54]. On top of the $E1$ strength function, the cross section calculation also depends on the adopted NLD. We have used here two versions of the HFB plus combinatorial model, namely, the original one from Ref. [55] and the latest version based on the temperature-dependent HFB model of Ref. [56]. Both of them are normalized to the experimental $s$-wave spacing $D_0$ values [54] whenever available.

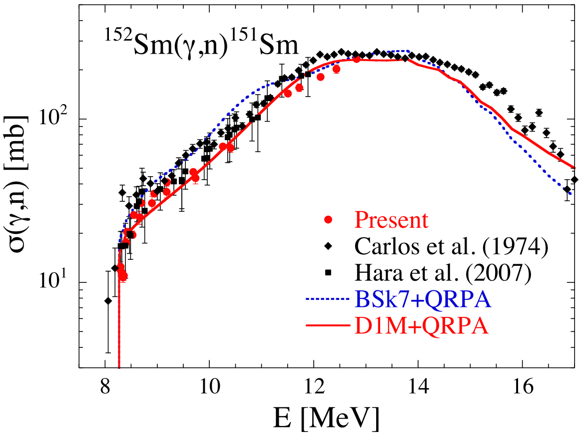

FIG. 13. (Color online) Same as Fig. 8 for $^{152}$Sm. Experimental $(\gamma,n)$ data from Ref. [29] are also included.

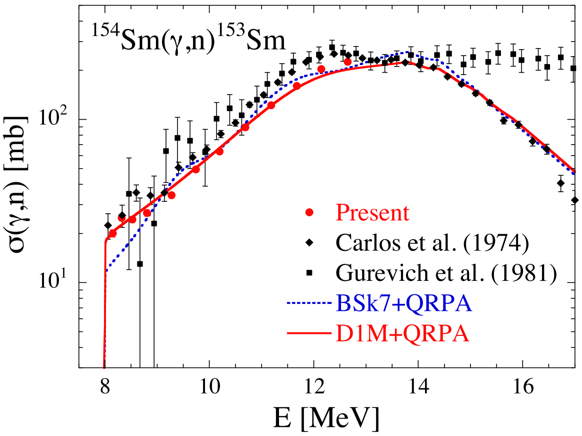

FIG. 14. (Color online) Same as Fig. 8 for $^{154}$Sm. Experimental photoabsorption data from Ref. [30] are also included.

As can be seen in Fig. 15, the TALYS calculation agrees well with experimental data for all six Sm isotopes, which shows that, within the uncertainties affecting the experimental $\gamma$SF and $D_0$ value, all $\gamma$SF data are compatible with both the photoabsorption above the threshold and the radiative capture channels below the threshold. Experimental data exist for the $^{151}$Sm$(n,\gamma)^{152}$Sm cross section and our predictions are in rather good agreement with the measurements. The corresponding TALYS Maxwellian-averaged cross section amounts, at the thermal energy of 30 keV, to 3200 ± 800 mb, where the uncertainty stems from the use of our two different NLD models [55,56]. This value is in agreement with the value of 3031 ± 68 mb found experimentally [13].

The $\gamma$SF method can now be applied to the experimentally unknown neutron capture cross section of $^{153}$Sm. The D1M+HFB $E1$ strength function positively tested on the photoneutron and radiative capture cross section is used. As far as the NLD is concerned, here also both versions of the HFB plus combinatorial models [55,56] are considered. No experimental information exists on the resonance spacing at the neutron binding energy for $^{154}$Sm. The major uncertainty in the estimate of the neutron capture cross section therefore stems from the adopted NLD model. The final prediction is shown in Fig. 16. The Japanese JENDL-4.0 and American ENDF/B-VII.1 evaluations [57] are seen to be in relatively good agreement with our estimate, but the Russian ROSFOND-2010 evaluation gives rather lower cross sections below 10 keV. The resulting Maxwellian-averaged cross section of astrophysical interest amounts, at 30 keV, to 1285 ± 360 mb. Our estimate (and, consequently, also the ENDF/B-VII.1 and JENDL-4.0 ones) is found to be larger than the theoretical Maxwellian-averaged cross sections of 1095 ± 175 mb recommended in Ref. [58].

## VI. CONCLUSIONS

Photoneutron cross sections were measured for all seven stable Sm isotopes near the neutron threshold with quasi-monochromatic laser-Compton scattering $\gamma$ rays. Our photoneutron cross sections are found to be about 20%–37%

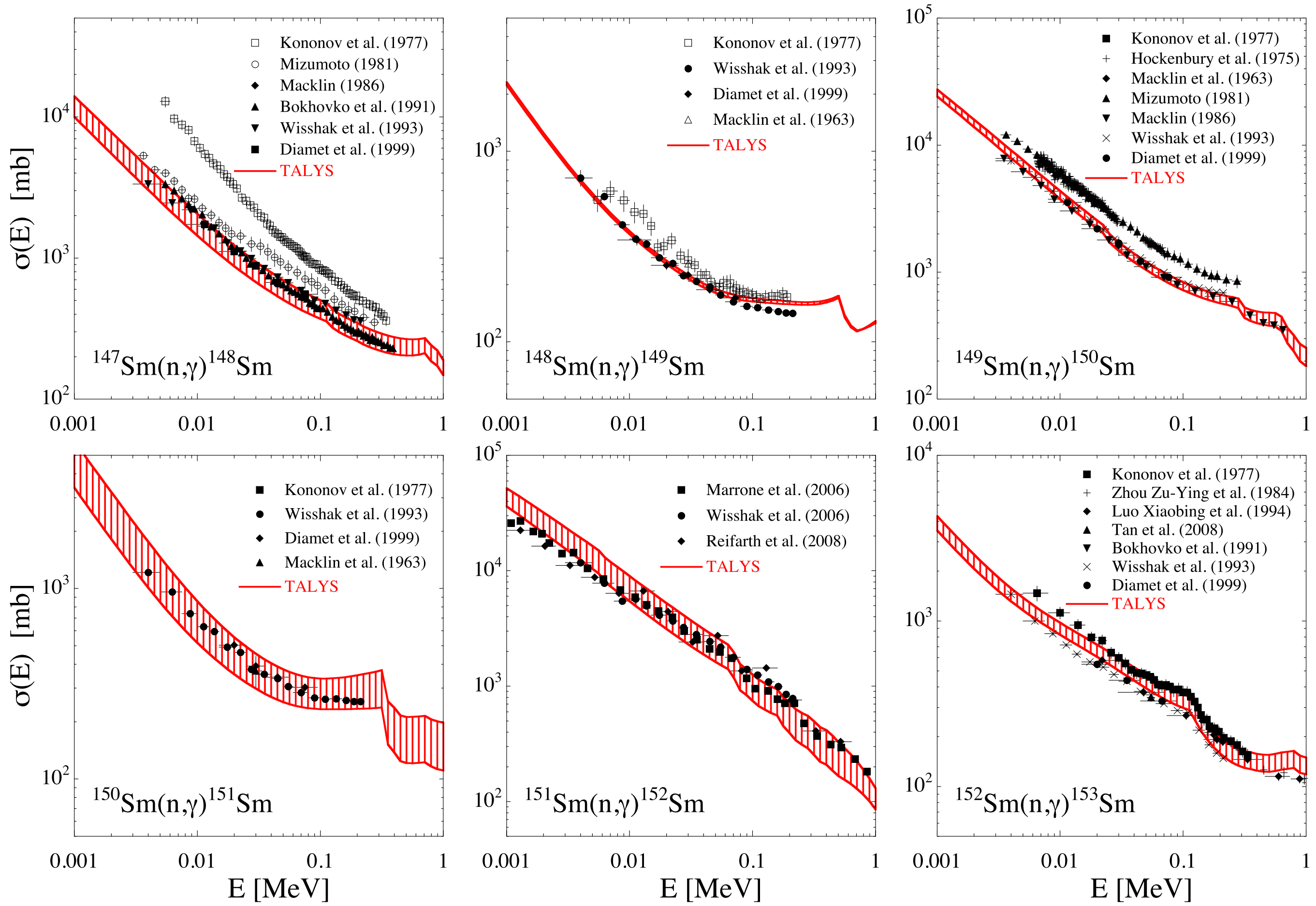

FIG. 15. (Color online) Comparison between the Sm measured radiative neutron capture cross sections [13,40–53] with a TALYS calculation making use of the D1M+QRPA calculation for the $E1$ strength. The hashed area corresponds to the sensitivity to the NLD.

lower relative to the 1974 measurements in Saclay [26]. The new data are analyzed with HFB+QRPA models of $E1$ $\gamma$-ray strength. The D1M+QRPA strength function is found to be able to reproduce fairly well the photodata in all the energy range above the neutron threshold and simultaneously the experimental neutron capture cross sections which are sensitive to the $\gamma$SF below the threshold. A thorough analysis of the reverse $(n,\gamma)$ cross sections is made including the radioactive nucleus $^{151}$Sm with a half-life 90 yr and $^{153}$Sm with a half-life 1.928 d through the $\gamma$-ray strength function method. While neutron capture measurements exist for $^{151}$Sm, the new constraint on the $^{154}$Sm $E1$ strength leads to a $^{153}$Sm$(n,\gamma)^{154}$Sm cross section sensitively higher than the one predicted in previous works.

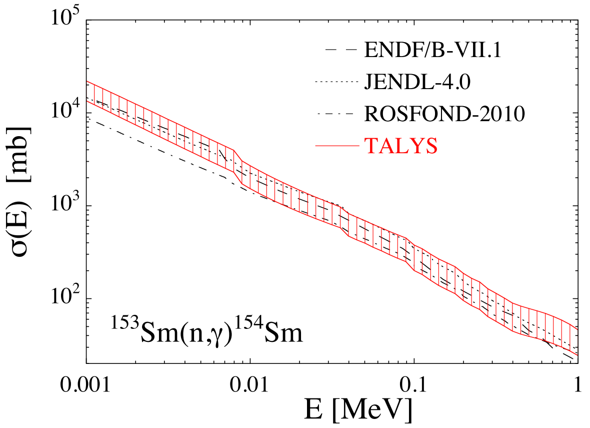

FIG. 16. (Color online) Prediction of the $^{153}$Sm$(n,\gamma)^{154}$Sm cross section. The dotted, dashed, and dashed-dotted curves correspond to the Japanese JENDL-4.0, American ENDF/B-VII.1, and Russian ROSFOND-2010 evaluations [57], respectively.

## ACKNOWLEDGMENTS

This work was supported by the Japan Private School Promotion Foundation and by the JSPS-FNRS bilateral program. We are grateful to M. Igashira of the Tokyo Institute of Technology for making the $^{148,149,152,154}$Sm samples available for the present experiment. We thank Florin Rotaru of the National Institute for Physics and Nuclear Engineering Horia Hulubei for initiating us into GEANT4 coding and for fruitful discussions. We acknowledge PRACE for awarding us access to the resource CURIE based in France at TGCC-CEA. D.M.F., I.G., and O.T. acknowledge financial support from the Extreme Light Infrastructure Nuclear Physics (ELI-NP) Phase I project, a project co-financed by the European Union through the European Regional Development Fund. H.T.N. and T.R. acknowledge financial support from the Norwegian Research Council (NFR), Project No. 210007. S.G. acknowledges the financial support from the FNRS.

[1] F. Käppeler, R. Gallino, S. Bisterzo, and W. Aoki, Rev. Mod. Phys. **83**, 157 (2011).
[2] IAEA-TECDOC-985, IAEA, November 1997.
[3] H. Utsunomiya *et al.*, Phys. Rev. C **80**, 055806 (2009).
[4] H. Utsunomiya *et al.*, Phys. Rev. C **82**, 064610 (2010).
[5] D. M. Brink, Ph.D. thesis, Oxford University, 1955.
[6] H. Utsunomiya *et al.*, Phys. Rev. C **81**, 035801 (2010).
[7] H. Utsunomiya *et al.*, Phys. Rev. C **84**, 055805 (2011).
[8] H. Utsunomiya *et al.*, Phys. Rev. C **88**, 015805 (2013).
[9] H. T. Nyhus *et al.* (unpublished)
[10] M. Arnould and S. Goriely, Phys. Rep. **384**, 1 (2003).
[11] M. Arnould, S. Goriely, and K. Takahashi, Phys. Rep. **450**, 97 (2008).
[12] U. Abbondanno *et al.*, Phys. Rev. Lett. **93**, 161103 (2004).
[13] K. Wisshak, F. Voss, F. Käppeler, M. Krtička, S. Raman, A. Mengoni, and R. Gallino, Phys. Rev. C **73**, 015802 (2006).
[14] S. Amano *et al.*, Nucl. Instrum. Phys. Res. A **602**, 337 (2009).
[15] H. Utsunomiya *et al.*, IEEE Trans. Nucl. Sci. **61**, 1252 (2014).
[16] J. Allison *et al.*, IEEE Trans. Nucl. Sci. **53**, 270 (2006).
[17] S. Agostinelli *et al.*, Nucl. Instrum. Phys. Res. A **506**, 250 (2003).
[18] I. Gheorghe *et al.* (unpublished).
[19] B. L. Berman and S. C. Fultz, Rev. Mod. Phys. **47**, 713 (1975).
[20] O. Itoh *et al.*, J. Nucl. Sci. Technol. **48**, 834 (2011).
[21] T. Kondo *et al.*, Nucl. Instrum. Phys. Res. A **659**, 462 (2011).
[22] T. Kii *et al.*, in *Proceedings of the 12th Symposium on Accelerator Science and Technology*, edited by Yasushige Yano (The Institute of Physical and Chemical Research (RIKEN), Wako, Japan, 1999), pp. 484–485.
[23] H. Toyokawa, T. Kii, H. Ohgaki, T. Shima, T. Baba, and Y. Nagai, IEEE Trans. Nucl. Sci. **47**, 1954 (2000).
[24] NIST Physical Measurement Laboratory, http://physics.nist.gov/PhysRefData/XrayMassCoef/tab3.html.
[25] H. Utsunomiya *et al.*, Phys. Rev. C **74**, 025806 (2006).
[26] P. Carlos, H. Beil, R. Bergere, A. Lepretre, A. Deminiac, and A. Veyssiere, Nucl. Phys. A **225**, 171 (1974).
[27] S. Goriely, E. Khan, and M. Samyn, Nucl. Phys. A **739**, 331 (2004).
[28] M. Martini, S. Hilaire, S. Goriely, A. J. Koning, and S. Péru, Nucl. Data Sheets **118**, 273 (2014).
[29] K. Y. Hara *et al.*, J. Nucl. Sci. Technol. **44**, 938 (2007).
[30] G. M. Gurevich, L. E. Lazareva, V. M. Mazur, S. Yu. Merkulov, G. V. Solodukhov, and V. A. Tyutin, Nucl. Phys. A **351**, 257 (1981).
[31] C. T. Angell *et al.*, Phys. Rev. C **86**, 051302(R) (2012).
[32] C. Nair *et al.*, Phys. Rev. C **81**, 055806 (2010).
[33] B. L. Berman, R. E. Pywell, S. S. Dietrich, M. N. Thompson, K. G. McNeill, and J. W. Jury, Phys. Rev. C **36**, 1286 (1987).
[34] A. J. Koning, S. Hilaire, and M. Duijvestijn, in *Nuclear Data for Science and Technology*, edited by O. Bersillon, F. Gunsing, E. Bauge, R. Jacqmin, and S. Leray (EDP Sciences, Les Ulis, France, 2008), p. 211.
[35] A. J. Koning and D. Rochman, Nucl. Data Sheets **113**, 2841 (2012).
[36] S. Péru and H. Goutte, Phys. Rev. C **77**, 044313 (2008).
[37] S. Péru and M. Martini, Eur. Phys. J. A **50**, 88 (2014).
[38] S. Goriely, S. Hilaire, M. Girod, and S. Péru, Phys. Rev. Lett. **102**, 242501 (2009).
[39] T. Kondo *et al.*, Phys. Rev. C **86**, 014316 (2012).
[40] V. N. Kononov, B. D. Jurlov, E. D. Poletaev, V. M. Timokhov, and G. N. Manturov, Yad. Konstanty **22**, 29 (1977).
[41] R. L. Macklin, N. W. Hill, J. A. Harvey, and G. L. Tweed, Phys. Rev. C **48**, 1120 (1993).
[42] M. Mizumoto, Nucl. Phys. A **357**, 90 (1981).
[43] R. Macklin, EXFOR database, https://www-nds.iaea.org/exfor.
[44] M. V. Bokhovko, V. N. Kononov, N. S. Rabotnov, A. A. Voevodskiy, G. N. Manturov, and V. M. Timokhov, Fiz.-Energ Institut, Obninsk, Report No. 2168, 1991.
[45] K. Wisshak, K. Guber, F. Voss, F. Käppeler, and G. Reffo, Phys. Rev. C **48**, 1401 (1993).
[46] B. Diamet, M. Igashira, M. Mizumachi, S. Mizuno, J.-I. Hori, K. Masuda, and T. Ohsaki, J. Nucl. Sci. Technol. **36**, 865 (1999).
[47] R. L. Macklin, J. H. Gibbons, and T. Inada, Nature (London) **197**, 369 (1963).
[48] R. W. Hockenbury, W. R. Koste, and R. A. Shaw, Bull. Am. Phys. Soc. **20**, 560 (1975).
[49] S. Marrone *et al.*, Phys. Rev. C **73**, 034604 (2006).
[50] R. Reifarth, T. A. Bredeweg, A. Couture, E.-I. Esch, and U. Greife, in *10th Symposium on Nuclei in the Cosmos*, edited by H. Schatz, S. Austin, T. Beers, Ed Brown, B. Lynch, and R. Zegers (SISSA, Trieste, Italy, 2008), p. 84.
[51] Z.-Y. Zhou, Y. Chen, S.-S. Jiang, and D.-X. Luo, Chin. J. Nucl. Phys. **6**, 174 (1984).
[52] X. Luo, Y. Xia, Z. Yang, and M. Liu, Chin. J. Nucl. Phys. **16**, 275 (1994).
[53] V. H. Tan, T. T. Anh, N. C. Hai, P. N. Son, and T. Fukahori, JAEA Conf. Proc. **006**, 40 (2008).
[54] R. Capote *et al.*, Nucl. Data Sheets **110**, 3107 (2009).
[55] S. Goriely, S. Hilaire, and A. J. Koning, Phys. Rev. C **78**, 064307 (2008).
[56] S. Hilaire, M. Girod, S. Goriely, and A. J. Koning, Phys. Rev. C **86**, 064317 (2012).
[57] Evaluated Nuclear Data Files, 2011, http://www-nds.iaea.or.at/exfor.htm.
[58] Z. Y. Bao, H. Beer, F. Käppeler, F. Voss, K. Wisshak, and T. Rauscher, At. Data Nucl. Data Tables **76**, 70 (2000).

PHYSICAL REVIEW C **91**, 015808 (2015)

# Photoneutron cross sections for neodymium isotopes: Toward a unified understanding of $(\gamma,n)$ and $(n,\gamma)$ reactions in the rare earth region

H.-T. Nyhus,[1] T. Renstrøm,[1] H. Utsunomiya,[2,3] S. Goriely,[4] D. M. Filipescu,[5] I. Gheorghe,[5,7] O. Tesileanu,[5] T. Glodariu,[6] T. Shima,[8] K. Takahisa,[8] S. Miyamoto,[9] Y.-W. Lui,[10] S. Hilaire,[11] S. Péru,[11] M. Martini,[4,11,12] L. Siess,[4] and A. J. Koning[13]

[1] *Department of Physics, University of Oslo, N-0316 Oslo, Norway*
[2] *Department of Physics, Konan University, Okamoto 8-9-1, Kobe 659-8501, Japan*
[3] *Center for Nuclear Study, University of Tokyo, 2-1 Hirosawa, Wako, Saitama 351-0198, Japan*
[4] *Institut d'Astronomie et d'Astrophysique, Université Libre de Bruxelles, Campus de la Plaine, CP-226, 1050 Brussels, Belgium*
[5] *ELI-NP, "Horia Hulubei" National Institute for Physics and Nuclear Engineering (IFIN-HH), 30 Reactorului, 077125 Bucharest-Magurele, Romania*
[6] *"Horia Hulubei" National Institute for Physics and Nuclear Engineering (IFIN-HH), 30 Reactorului, 077125 Bucharest-Magurele, Romania*
[7] *Faculty of Physics, University of Bucharest, RO-077125, Bucharest, Romania*
[8] *Research Center for Nuclear Physics, Osaka University, Suita, Osaka 567-0047, Japan*
[9] *Laboratory of Advanced Science and Technology for Industry, University of Hyogo, 3-1-2 Kouto, Kamigori, Ako-gun, Hyogo 678-1205, Japan*
[10] *Cyclotron Institute, Texas A&M University, College Station, Texas 77843, USA*
[11] *CEA, DAM, DIF, F-91297 Arpajon, France*
[12] *Department of Physics and Astronomy, Ghent University, Proeftuinstraat 86, B-9000 Gent, Belgium*
[13] *Nuclear Research and Consultancy Group, P.O. Box 25, NL-1755 ZG Petten, The Netherlands*

(Received 3 October 2014; revised manuscript received 20 November 2014; published 22 January 2015)

Photoneutron cross sections were measured for five stable Nd isotopes, $^{143,144,145,146,148}$Nd, near neutron threshold with highly monochromatic laser-Compton scattering $\gamma$ rays. The photoneutron data were compared with the calculations performed with the TALYS reaction code with inputs of the Skyrme Hartree-Fock-Bogoliubov (HFB) plus quasi-particle random phase approximation (QRPA) model and the axially symmetric deformed Gogny HFB plus QRPA model of $E1$ $\gamma$-ray strength. Using the $\gamma$-ray strength function constrained by the present photoneutron data, a thorough analysis of the reverse $(n,\gamma)$ cross sections is made. Radiative neutron capture cross sections for an s-process branching-point nucleus in the rare earth region, $^{147}$Nd with the half-life 10.98 d, are deduced with the $\gamma$-ray strength function method. The impact of the newly evaluated $^{147}$Nd$(n,\gamma)^{148}$Nd cross section on s-process nucleosynthesis is discussed.

DOI: 10.1103/PhysRevC.91.015808 PACS number(s): 25.20.Lj, 21.10.Pc, 25.40.Lw, 27.60.+j

## I. INTRODUCTION

Radiative neutron capture on nuclei along the line of $\beta$ stability in the medium- to heavy-mass region of the chart of nuclei is an important issue in nuclear astrophysics and nuclear engineering. In nuclear astrophysics, the cross sections are important to determine the s-process path at branching points where neutron capture and $\beta$ decay compete [1]. The neutron capture data are also of essential importance for nuclear transmutation of long-lived fission products known as nuclear waste in the field of nuclear engineering [2]. Following the preceding paper for samarium isotopes [3], this paper for neodymium isotopes constitutes the second part of our investigations in the rare earth region.

Although experimental data of radiative neutron capture cross sections for stable nuclei are well documented [4], those for radioactive nuclei are scarce due to the difficulty of direct measurements that requires both an intense neutron beam and radioactive samples. While some of radioactive nuclei with half-lives ($T_{1/2}$) of the order of years have become objectives for direct measurements, for example, $^{151}$Sm ($T_{1/2} = 90$ yr) [5,6] and $^{63}$Ni ($T_{1/2} = 100$ yr) [7] at CERN/n-TOF, $^{147}$Pm ($T_{1/2} = 2.62$ yr) at Karlsruhe [8], $^{244}$Cm ($T_{1/2} = 18.1$ yr) [9] at J-Parc (Tokai), and $^{173}$Lu ($T_{1/2} = 1.73$ yr) [10] in progress at LANSCE (Los Alamos), those with $T_{1/2}$ of the order of days and shorter are far beyond the experimental scope at present.

The well-established $\gamma$-ray strength function ($\gamma$SF) method can be used for constraining the $(n,\gamma)$ cross sections for radioactive nuclei [11,12]. Relying on the Brink hypothesis [13] linking the photo-deexcitation process to photoabsorption, the method determines the $\gamma$SF which commonly quantifies radiative neutron capture and photoneutron cross sections. The $(n,\gamma)$ cross section is governed by primary $\gamma$ transitions from a neutron capture state at the excitation energy $E$ to all possible nuclear states below the neutron threshold. Thus, the $\gamma$SF at $\gamma$-ray energies $\varepsilon_\gamma$ below the neutron separation energy ($S_n$) and the nuclear level density at the final state ($E - \varepsilon_\gamma$) play an essential role in this capture reaction [14]. Photoneutron cross sections provide a stringent experimental constraint in absolute scale on the $\gamma$SF around $S_n$. When auxiliary $(\gamma,\gamma')$ and particle-$\gamma$ coincidence data that help to construct the $\gamma$SF below $S_n$ are unavailable, the method requires a systematic measurement of photoneutron cross sections for neighboring stable isotopes of the radioactive nucleus of interest, in addition to existing $(n,\gamma)$ data that serve as experimental constraints on the $\gamma$SF below $S_n$. Thus, a unified understanding of $(n,\gamma)$ and $(\gamma,n)$ cross sections throughout an isotopic chain offers detailed information on the $\gamma$SF for a given nucleus formed by neutron capture on the radioactive nucleus. Such a systematic approach with the $\gamma$SF method has been applied to zirconium [15], tin [16], and molybdenum [17] isotopes.

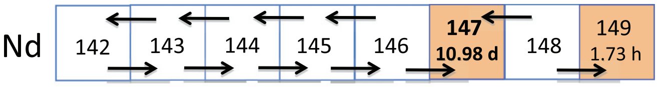

FIG. 1. (Color online) The chart of nuclei depicting our systematic analysis of $(\gamma,n)$ and $(n,\gamma)$ cross sections for Nd isotopes in the context of the $\gamma$-ray strength function method. Photoneutron cross sections measured in the present experiment are shown by left-pointing arrows. Radiative neutron capture cross sections discussed in the present systematic analysis are shown by right-pointing arrows. Photoneutron cross sections for the radioactive nucleus $^{147}$Nd are deduced with the $\gamma$-ray strength function method.

Figure 1 depicts photoneutron emission (←) and radiative neutron capture (→) on Nd isotopes of interest in the present paper. We measured photoneutron cross sections for five neodymium isotopes, $^{143\text{–}146,148}$Nd. Combining the present $(\gamma,n)$ data with existing $(n,\gamma)$ data for six Nd isotopes, $^{142\text{–}146,148}$Nd, we determine $^{147}$Nd$(n,\gamma)$ cross sections with the $\gamma$SF method. The present systematic measurement included two odd-$A$ nuclei, $^{143}$Nd and $^{145}$Nd, for which photoneutron cross sections are presented near the neutron threshold for the first time.

In this paper, we present radiative neutron capture cross sections for $^{147}$Nd with $T_{1/2} = 10.98$ d, an s-process branching-point nucleus located in the rare earth region [1,18]. Its $\beta$ decay leads to the subsequent branchings at $^{147,148}$Pm [8], which in turn affect the s-process production ratio of $^{147}$Sm to $^{148}$Sm. We discuss a possible impact of the new cross section for $^{147}$Nd on the abundance ratio of $^{148}$Nd to the s-only nucleus $^{148}$Sm in asymptotic giant branch (AGB) stars.

The outline of the paper is given as follows. A description of the experimental procedure and the data reduction is limited to a minimum in Sec. II, yielding a detailed description to the preceding paper [3]. The theoretical analysis of the photoneutron cross sections is given in Sec. III. The radiative neutron cross sections are analyzed in Sec. IV. The $^{147}$Nd$(n,\gamma)^{148}$Nd cross section is determined with the $\gamma$SF method in Sec. V, followed by a possible impact of the cross section on the s-process nucleosynthesis in Sec. VI. Finally, conclusions are drawn in Sec. VII.

## II. EXPERIMENT

The experiment was performed at the experimental hutch GACKO (Gamma Collaboration Hutch of Konan University) of the $\gamma$-ray beamline BL01 of the NewSUBARU synchrotron radiation facility [19]. In the BL01, energy-tunable and highly monochromatic $\gamma$-ray beams [20] are produced through inverse Compton scattering between Nd : YVO$_4$ laser photons ($\lambda = 1064$ nm) and relativistic electrons in the NewSUBARU storage ring. Fine pencil-like beams of the laser Compton scattering (LCS) $\gamma$ rays were produced and measured with a $3.5'' \times 4.0''$ LaBr$_3$(Ce) detector. The response function of the LaBr$_3$(Ce) detector to the LCS $\gamma$ rays was reproduced with a GEANT4 simulation code implemented with the kinematics of the laser inverse Compton scattering to obtain the energy distribution of the $\gamma$-ray beam. The energy spread of the LCS $\gamma$-ray beam with a low-energy tail was 1%–2% in full width at half maximum (see Figs. 4 and 5 of [3]). Details of the GEANT4 simulation will be given in a forthcoming paper [21], where also a more in-depth description of the experimental setup can be found.

Samples of $^{143\text{–}146,148}$Nd enriched to 90.85%–98.07% all in the oxide form of Nd$_2$O$_3$ with areal densities of 1.35–2.78 g/cm$^2$ were encapsulated in pure-aluminum containers and irradiated with LCS $\gamma$-ray beams. The samples were dehydrated by baking at temperatures up to 393 °C for 4 h in vacuum before being placed inside the aluminum containers. The sample masses were determined by weighing the containers before and after the filling.

The $\gamma$-rays flux was determined by the pile-up method of Ref. [22] after detecting the beam with a $6'' \times 5''$ NaI(Tl) detector mounted at the end of the beamline. Typically 20% corrections were made for the transmission rate of the LCS $\gamma$ rays through the NaI(Tl) detector.

Neutrons were detected with a high-efficiency $4\pi$ neutron detector consisting of 20 $^3$He proportional counters embedded in a polyethylene moderator of $36 \times 36 \times 50$ cm$^3$ fully covered by additional 5-cm-thick polyethylene plates with 1-mm-thick cadmium for background neutron suppression. Neutrons were moderated in the polyethylene before being detected with three rings of 4, 8, and 8 $^3$He counters placed at distances of 3.8, 7.0, and 10.0 cm, respectively from the $\gamma$-ray beam axis. The average neutron energy was determined by the so-called ring-ratio technique originally developed by Berman and Fultz [23]. The total neutron detection efficiency is more than 60% for neutrons with energies less than 1 MeV. More details of the neutron detection can be found in Ref. [24]. Neutron detection efficiencies of the three rings were remeasured after the present experiment using a calibrated $^{252}$Cf source with an emission rate of $2.27 \times 10^4$ s$^{-1}$ with 2.2% uncertainty at the National Metrology Institute of Japan. The measurement excellently reproduced the results obtained at the same institute in 2006.

Photoneutron cross sections are deduced with the Taylor expansion method [25], which takes into account the energy spread of the LCS $\gamma$-ray beam. Corrections were also made for the contributions to the cross section coming from the isotopic impurities in the Nd samples. The correction remains small, being 1%–7% for the energy spread of the highly monochromatic LCS $\gamma$-ray beam and 2% even for the isotopic impurities of the less-enriched (90.85% and 91.73%) $^{143,145}$Nd samples. The systematic uncertainty of the present cross sections is 4.4% with the breakdown of 3% in the photon flux and 3.2% in the neutron detection efficiency.

Our photoneutron cross sections are compared in Fig. 2 with the Saclay measurements [26]. While a good agreement is obtained in the $^{146,148}$Nd cases, significant discrepancies are observed for the light Nd isotopes. In particular, our experiment leads to cross sections lower by typically 30% for $^{143}$Nd, 20% for $^{144}$Nd, and 27% for $^{145}$Nd. Such an overestimate by the Saclay photodata was also reported in previous comparisons for $^{142}$Nd with a renormalization by 0.86 [27], for $^{144}$Sm by 0.80 [28], and for $^{\text{nat}}$Rb, $^{\text{nat}}$Sr, $^{89}$Y, $^{90}$Zr, $^{93}$Nb, $^{127}$I, $^{197}$Au, and $^{208}$Pb by a factor of 0.80–0.93 [29].

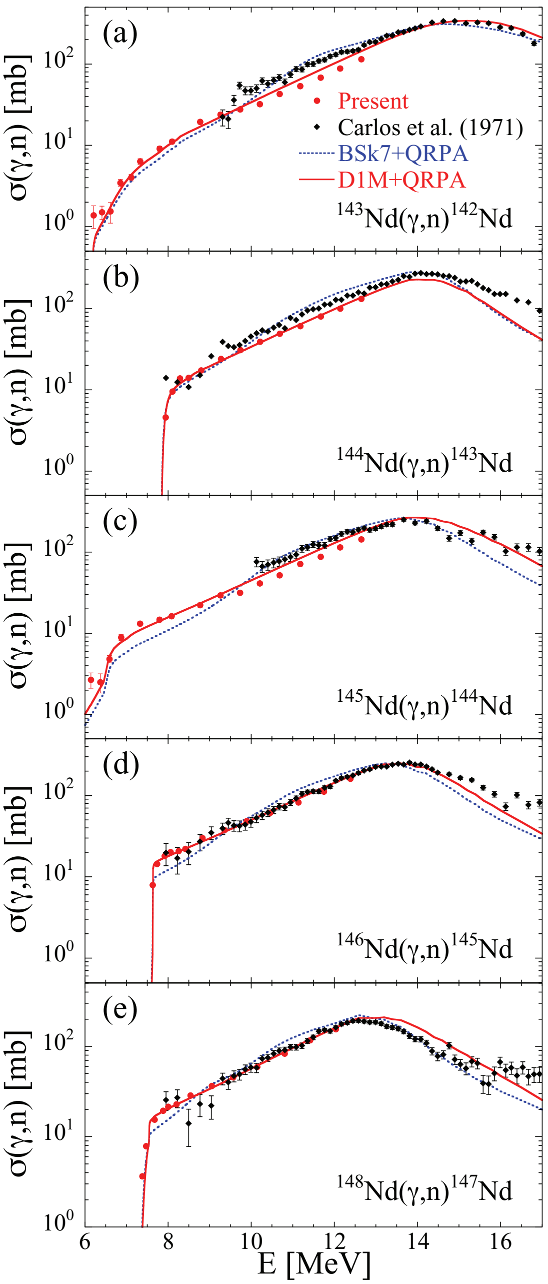

FIG. 2. (Color online) Comparison between the present photoneutron emission cross sections and previously measured ones [26] for $^{143-146,148}$Nd. Also included are the predictions from Skyrme HFB + QRPA (based on the BSk7 interaction) [32] and axially deformed Gogny HFB + QRPA models (based on the D1M interaction) [34].

## III. THEORETICAL ANALYSIS

### A. Photoneutron cross sections

Our new photoneutron cross sections shown in Fig. 2 have been compared to theoretical calculations obtained with the TALYS nuclear reaction code [30,31] and two different models of the $\gamma$SF, namely, the Skyrme Hartree-Fock-Bogoliubov (HFB) plus quasi-particle random phase approximation (QRPA) model [32] based on the BSk7 interaction and the axially symmetric deformed Gogny HFB plus QRPA model [33–35] based on the D1M interaction [36]. The BSk7+QRPA model introduces phenomenological corrections to take the damping of the collective motion as well as the deformation effects into account. (Note, however, that deformation parameters are consistently extracted from the HFB-7 mass model based on the BSk7 Skyrme functional [37].) In contrast, the D1M + QRPA model allows for a consistent description of axially symmetric deformations and includes phenomenologically the impact of multiparticle-multihole configurations as a function of their densities [34]. Both models have proven their capacity to reproduce experimental photoabsorption data relatively well.

As seen in Fig. 2, cross sections around the neutron threshold are rather well described by the D1M + QRPA model, although some deviations can be seen. The agreement around the neutron threshold is rather satisfactory and there is no reason to invoke the presence of extra low-lying strength from the present data, at least in the vicinity of the neutron threshold, as seen in some previous photodata [11,15,16,38]. In contrast, larger deviations are seen for the predictions obtained with the BSk7 + QRPA strength, in particular around 11 MeV, but also at lower energies in the $^{145,146}$Nd cases.

### B. Radiative neutron capture cross sections

We now turn to the reverse radiative neutron capture channel. It should be kept in mind that the corresponding cross section for incident keV neutrons depends sensitively on the $\gamma$SF, but in a rather lower energy range below the neutron threshold, typically around 6 MeV of $\gamma$-ray energy. The predicted tail of the $\gamma$SF at low energies therefore plays a fundamental role.

On the basis of the Gogny HFB plus QRPA $\gamma$-ray strength [34], the reverse radiative neutron capture cross sections are now estimated with the TALYS reaction code [30,31] for the stable and experimentally known $^{142-146,148}$Nd isotopes and compared with experimental cross sections in Fig. 3. In addition to the $E1$ strength function, the cross section calculation also depends on the adopted nuclear level density. We have used here the temperature-dependent HFB plus combinatorial model [39] normalized to the experimental s-wave spacing $D_0$ values at the neutron binding energy [14]. Note that experimental s-wave spacings are available, so uncertainties related to the adopted NLD model are rather small, typically 10%, as shown in Fig. 3, where the hashed areas correspond to uncertainties on experimental $D_0$ values. Similarly, the uncertainties related to the adopted neutron optical potential are negligible in the energy range of astrophysical interest, i.e., in the keV–MeV region.

Based on the radiative neutron capture cross section, the laboratory (i.e., without including the contribution of excited states) Maxwellian-averaged cross sections (MACS) have been estimated and compared with experimental data at an energy of $kT = 30$ keV in Table I. The theoretical error bars stem from the NLD uncertainties affecting the $D_0$ values. Here also, our TALYS predictions are compatible with experimental data, with theoretical values being usually higher than the measurements, except in the $^{142}$Nd and $^{144}$Nd cases.

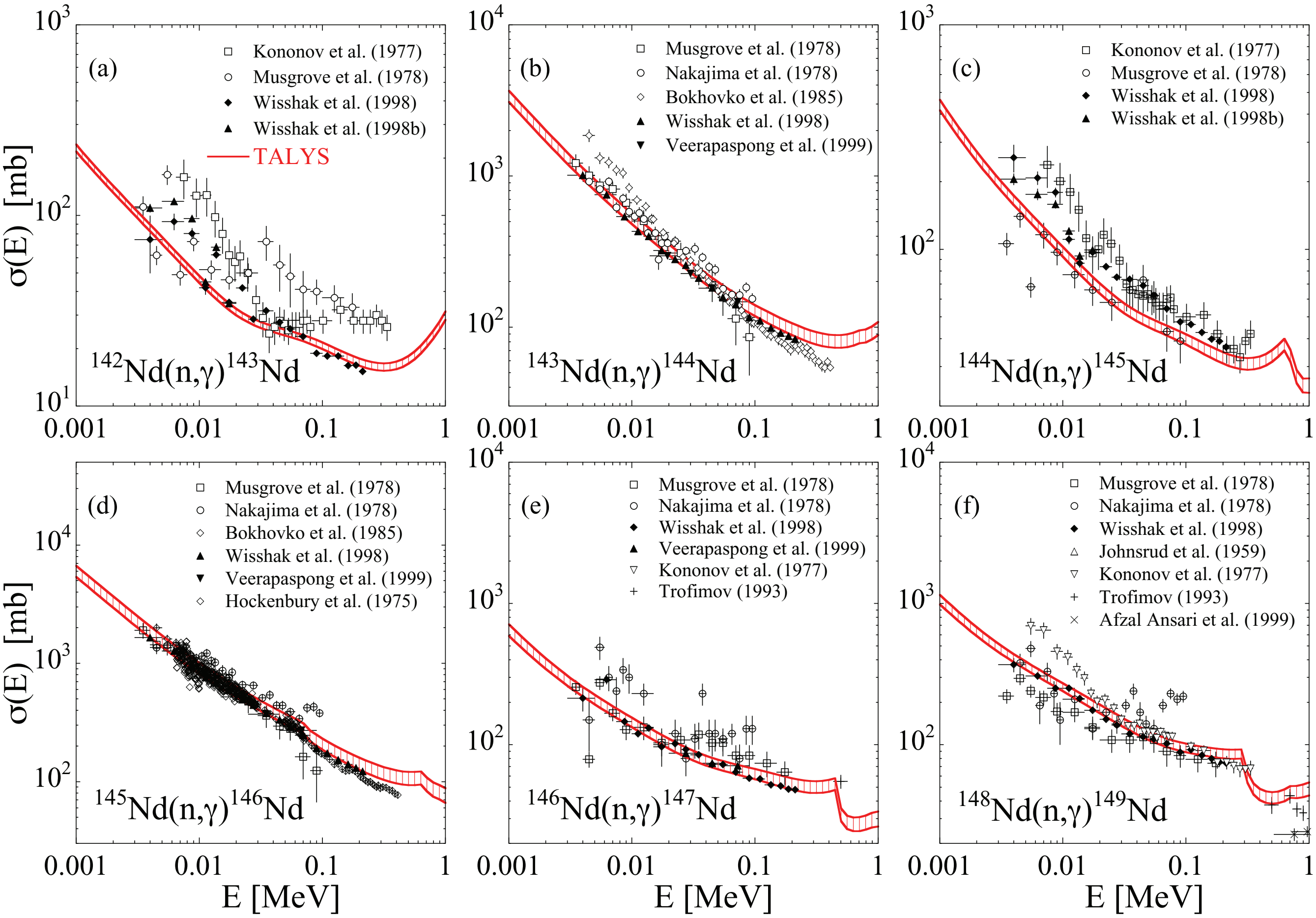

FIG. 3. (Color online) Comparison between the measured radiative neutron capture cross sections [40–50] with TALYS calculations making use of the D1M + QRPA $E1$ strength (solid line). The hashed area corresponds to uncertainties related to the NLD model and their normalization on experimental s-wave spacings at the neutron binding energy.

It should however be stressed that the MACS [42,43] have been measured relative to the radiative neutron capture cross section of $^{197}$Au, which has been recently re-evaluated and found to deviate systematically by more than 5% from the cross section that is recommended as a reference for astrophysical applications [51].

As a conclusion, the TALYS calculation agrees well with the most recent experimental data for all six stable Nd isotopes, which shows that, within the uncertainties affecting the experimental $\gamma$SF and $D_0$ value, all $\gamma$SF data are compatible with both the photoabsorption above the threshold and the radiative capture channels below the threshold.

TABLE I. Comparison of experimental (laboratory) MACS of stable Nd isotopes [42,43] with the TALYS predictions at an energy of 30 keV. MACS are given in millibarns.

| Target | Exp. [42,43] | TALYS |
|---|---|---|
| $^{142}$Nd | 35.0 ± 0.7 | 31 ± 2 |
| $^{143}$Nd | 245 ± 3 | 267 ± 23 |
| $^{144}$Nd | 81.3 ± 1.5 | 63 ± 4 |
| $^{145}$Nd | 425 ± 5 | 478 ± 50 |
| $^{146}$Nd | 91.2 ± 1 | 96 ± 8 |
| $^{148}$Nd | 147 ± 2 | 157 ± 11 |

### C. Determination of the $^{147}$Nd$(n,\gamma)^{148}$Nd cross section

The $\gamma$SF method can now be applied to the experimentally unknown cross section $^{147}$Nd$(n,\gamma)^{148}$Nd by making use of the same nuclear inputs. In the case of $^{148}$Nd, experimental information exists on the resonance spacing at the neutron binding energy, namely, $D_0 = 4.0 \pm 1.5$ eV [14]. The 40% error on $D_0$ corresponds to the major uncertainty still affecting the prediction of the $^{147}$Nd$(n,\gamma)^{148}$Nd cross section, giving rise to a range of predicted cross sections within typically 20%–30%, as shown in Fig. 4. The ENDF/B-VII.1 evaluation [52] is seen to be in relatively good agreement with our estimate, but the ROSFOND-2010 evaluation [53] gives rather lower cross sections above typically a few keV and the JENDL-4.0 evaluation [54] gives larger values above typically 100 keV. The resulting MACS of astrophysical interest are shown in Fig. 5 and compared with the theoretical determination recommended in Ref. [55]. Our MACS (and, consequently, also the ENDF/B-VII.1 and JENDL-4.0 ones) are found to be significantly larger than those of the previous recommendation [55]. In particular, at 30 keV, our cross section

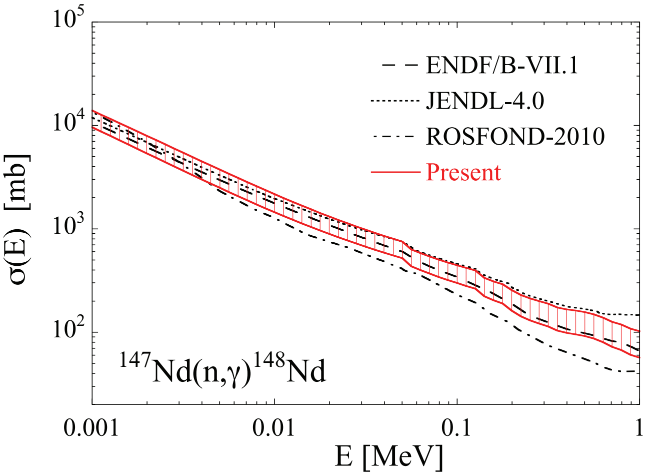

FIG. 4. (Color online) Prediction of the $^{147}\text{Nd}(n,\gamma)^{148}\text{Nd}$ cross section. The dotted, dashed, and dash-dotted curves correspond to the JENDL-4.0 [54], ENDF/B-VII.1 [52], and ROSFOND-2010 [53] evaluations.

amounts to 880 ± 170 mb, to be compared with 544 ± 90 mb recommended in Ref. [55] and theoretical values ranging between 387 and 663 mb from various statistical model calculations and compiled in the KADONIS library [56].

## IV. APPLICATION TO s-PROCESS NUCLEOSYNTHESIS IN AGB STARS

Even though the observation of radioactive Tc in stellar envelopes [57] clearly proves that the s-process takes place during the hydrostatic burning phases of a star, it remains difficult to explain the origin of the large neutron concentrations required to produce s elements. Two nuclear reactions are suggested as possible neutron sources, i.e., $^{13}\text{C}(\alpha,n)^{16}\text{O}$ and $^{22}\text{Ne}(\alpha,n)^{25}\text{Mg}$. These reactions could be responsible for a large production of neutrons during the given burning phases, namely, the core He-burning of massive stars (heavier than $10M_\odot$) and the shell He-burning during the thermal AGB instabilities (thermal pulses) of low- and intermediate-mass stars ($<10M_\odot$) [1,58]. The core He-burning of solar-metallicity stars has proved its ability to produce the lightest s elements (i.e., $70 \lesssim A \lesssim 90$), but since $^{22}$Ne is a secondary source, the efficiency remains identical for metal-poor stars. The astrophysical models underlying the thermal pulse scenario (believed to be responsible for the production of the $A > 90$ s elements) remain quite uncertain in many respects, in particular in the description of the mixing mechanisms that could be at the origin of the neutron production. AGB models including diffusive overshoot or rotational effects suggest the partial mixing of protons (PMP) from the H-rich envelope into the C-rich layers during the third dredge-up [59–61]. In low-mass AGB stars of typically 1 to $3M_\odot$, this PMP model has been successful in explaining the main and strong components of the s-process, including the production of Nd and Sm isotopes. In more massive AGB stars, such an s-process during the interpulse might be inhibited due to the high temperatures encountered at the base of the convective envelope and the resulting combustion of protons during the partial mixing [62]; the large temperatures can however lead to a significant neutron irradiation within the convective thermal pulse due to the activation of the $^{22}\text{Ne}(\alpha,n)^{25}\text{Mg}$ reaction [63].

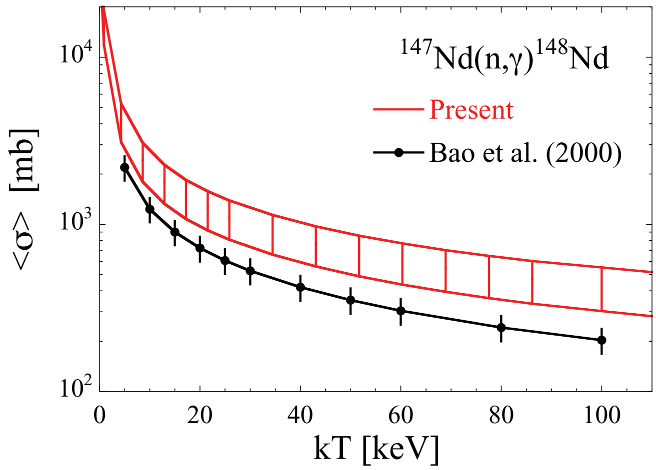

FIG. 5. (Color online) Comparison between our newly determined $^{147}\text{Nd}(n,\gamma)^{148}\text{Nd}$ MACS with the values recommended in Ref. [55].

Based on measured Maxwellian-averaged neutron capture cross sections of the stable Nd nuclei, the production of Nd and Sm isotopes by the s-process has already been studied in detail [8,42,43,64]. Our new estimation of the $^{147}\text{Nd}(n,\gamma)^{148}\text{Nd}$ cross section may however affect the s-process production of the sr nucleus $^{148}$Nd and the s-only $^{148}$Sm. To illustrate the impact of the newly determined MACS,

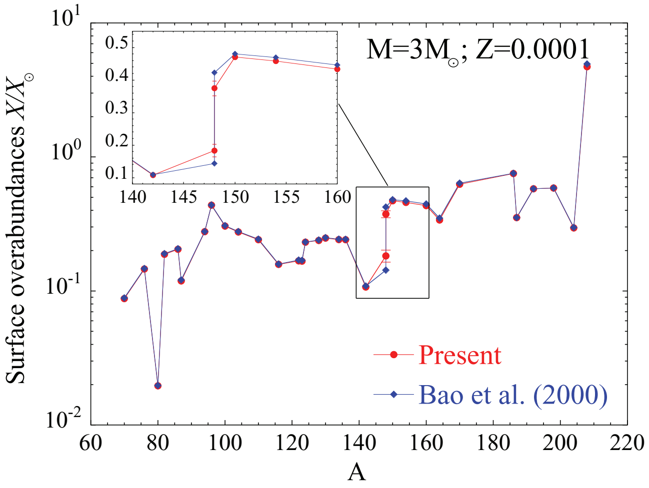

FIG. 6. (Color online) Final surface abundances $X$ for a $3M_\odot$ AGB model star of metallicity $Z = 0.0001$ with respect to the solar values $X_\odot$ for all s-only nuclei and $^{148}$Nd as a function of the mass number $A$. The circles (including error bars) are obtained with the present $^{147}\text{Nd}(n,\gamma)^{148}\text{Nd}$ MACS and the diamonds with the values given in Ref. [55]. The insert shows an enlargement of the $140 \leqslant A \leqslant 160$ region.

nucleosynthesis calculations have been performed within the PMP model [61] in $3M_\odot$ AGB model stars for three different metallicities, namely, $Z = Z_\odot = 0.0123$, $Z = 0.004$, and $Z = 0.0001$ [65]. Our upper value for the $^{147}$Nd$(n,\gamma)^{148}$Nd cross section, which is about twice as large as the one quoted in the widely used compilation of Ref. [55], leads to a larger production of $^{148}$Nd by 40% and a corresponding reduction in $^{148}$Sm production by about 10%. The final surface overabundances for the low-metallicity $Z = 0.0001$ star are illustrated in Fig. 6. In this specific case, if we use the upper limit of the cross section, we end up with an abundance ratio $[^{148}\mathrm{Nd}/^{148}\mathrm{Sm}] = \log[X(^{148}\mathrm{Nd})/X_\odot(^{148}\mathrm{Nd})] - \log[X(^{148}\mathrm{Sm})/X_\odot(^{148}\mathrm{Sm})] = -0.24$ (where $X$ is the mass fraction), while the previously used rate [55] gives $-0.47$. In other words, in low-metallicity stars, $^{148}$Nd can be relatively produced with respect to the s-only nucleus $^{148}$Sm, but also production could be significantly greater with our new upper limit, as seen in Fig. 6. In the case of the $Z = 0.004$ and $Z = Z_\odot$ model stars, we find a significantly lower production of $^{148}$Nd with respect to $^{148}$Sm, namely, $[^{148}\mathrm{Nd}/^{148}\mathrm{Sm}] = -0.46$ and $-0.64$, respectively, with our rate and $-0.68$ and $-0.82$, respectively, with the low rate of Ref. [55].

## V. CONCLUSIONS

The $\gamma$SF method has been applied to the Nd isotopic chain in order to determine the radiative neutron capture cross section of the unstable $^{147}$Nd isotope of astrophysical interest. Based on an extensive analysis of five newly measured photoneutron cross sections and the inverse radiative neutron capture cross sections, the nuclear reaction ingredients have been constrained, leading to a final $^{147}$Nd$(n,\gamma)^{148}$Nd cross section about 60% larger than the unconstrained value adopted in nucleosynthesis calculations. Our new rate determination leads to an increase of $^{148}$Nd production and a decrease of the s-only $^{148}$Sm abundance by the s-process in AGB stars.

## ACKNOWLEDGMENTS

This work was supported by the Japan Private School Promotion Foundation and partly by the JSPS-FNRS bilateral program. We are grateful to M. Igashira of the Tokyo Institute of Technology for making the $^{143,145,146}$Nd samples available to the present experiment. We thank Florin Rotaru of the National Institute for Physics and Nuclear Engineering Horia Hulubei for initiating us into GEANT4 coding and for fruitful discussions. We acknowledge PRACE for awarding us access to the resource CURIE based in France at TGCC-CEA. D. M. Filipescu, O. Tesileanu and I. Gheorghe acknowledge financial support from the Extreme Light Infrastructure Nuclear Physics (ELI-NP) Phase I, a project co-financed by the Romanian Government and the European Union through the European Regional Development Fund (425/12.12.2012, POS CCE, ID 1334 SMIS-CSNR 40741). H.-T. Nyhus and T. Renstrøm acknowledge financial support from the Norwegian Research Council (NFR), Project No. 210007. S. Goriely acknowledges financial support from the F.N.R.S.

---

[1] F. Käppeler, R. Gallino, S. Bisterzo, and W. Aoki, Rev. Mod. Phys. **83**, 157 (2011).
[2] IAEA-TECDOC-985, IAEA report, November 1997.
[3] D. M. Filipescu *et al.*, Phys. Rev. C **90**, 064616 (2015).
[4] https://www-nds.iaea.org/exfor/exfor.htm
[5] K. Wisshak, F. Voss, F. Käppeler, M. Krtička, S. Raman, A. Mengoni, and R. Gallino, Phys. Rev. C **73**, 015802 (2006).
[6] S. Marrone *et al.*, Phys. Rev. C **73**, 034604 (2006).
[7] C. Lederer *et al.*, Phys. Rev. C **89**, 025810 (2014).
[8] R. Reifarth *et al.*, Astrophys. J. **582**, 1251 (2003).
[9] A. Kimura *et al.*, J. Nucl. Sci. Technol. **49**, 708 (2012).
[10] https://www.oecd-nea.org/science/wpec/meeting2014/Exp_USA.pdf
[11] H. Utsunomiya *et al.*, Phys. Rev C **80**, 055806 (2009).
[12] H. Utsunomiya *et al.*, Phys. Rev C **82**, 064610 (2010).
[13] D. M. Brink, Ph.D thesis, Oxford University, 1955.
[14] R. Capote *et al.*, Nucl. Data Sheets **110**, 3107 (2009).
[15] H. Utsunomiya *et al.*, Phys. Rev. C **81**, 035801 (2010).
[16] H. Utsunomiya *et al.*, Phys. Rev C **84**, 055805 (2011).
[17] H. Utsunomiya *et al.*, Phys. Rev C **88**, 015805 (2013).
[18] M. Wiescher, F. Käppeler, and K. Langanke, Annu. Rev. Astron. Astrophys. **50**, 165 (2012).
[19] S. Amano *et al.*, Nucl. Instrum. Methods Phys. Res. A **602**, 337 (2009).
[20] K. Horikawa, S. Miyamoto, S. Amano, and T. Mochizuki, Nucl. Instrum. Methods Phys. Res. A **618**, 209 (2010).
[21] I. Gheorghe *et al.* (unpublished).
[22] T. Kondo *et al.*, Nucl. Instrum. Methods A **659**, 462 (2011).
[23] B. L. Berman and S. C. Fultz, Rev. Med. Phys. **47**, 713 (1975).
[24] O. Itoh *et al.*, J. Nucl. Sci. Technol. **48**, 834 (2011).
[25] H. Utsunomiya *et al.*, Phys. Rev. C **74**, 025806 (2006).
[26] P. Carlos, H. Beil, R. Bergere, A. Lepretre, and A. Veyssiere, Nucl. Phys. A **172**, 437 (1971).
[27] C. T. Angell *et al.*, Phys. Rev. C **86**, 051302(R) (2012).
[28] C. Nair *et al.*, Phys. Rev. C **81**, 055806 (2010).
[29] B. L. Berman, R. E. Pywell, S. S. Dietrich, M. N. Thompson, K. G. McNeill, and J. W. Jury, Phys. Rev. C **36**, 1286 (1987).
[30] A. J. Koning, S. Hilaire, and M. Duijvestijn, in *Nuclear Data for Science and Technology*, edited by O. Bersillon, F. Gunsing, E. Bauge, R. Jacqmin, and S. Leray (EDP Sciences, Les Ulis, France, 2008), p. 211.
[31] A. J. Koning and D. Rochman, Nucl. Data Sheets **113**, 2841 (2012).
[32] S. Goriely, E. Khan, and M. Samyn, Nucl. Phys. A **739**, 331 (2004).
[33] S. Péru and H. Goutte, Phys. Rev. C **77**, 044313 (2008).
[34] M. Martini, S. Hilaire, S. Goriely, A. J. Koning, and S. Péru, Nucl. Data Sheets **118**, 273 (2014).
[35] S. Péru and M. Martini, Eur. Phys. J. A **50**, 88 (2014).
[36] S. Goriely, S. Hilaire, M. Girod, and S. Péru, Phys. Rev. Lett. **102**, 242501 (2009).
[37] S. Goriely, M. Samyn, M. Bender, and J. M. Pearson, Phys. Rev. C **68**, 054325 (2003).
[38] T. Kondo *et al.*, Phys. Rev. C **86**, 014316 (2012).

[39] S. Hilaire, M. Girod, S. Goriely, and A. J. Koning, Phys. Rev. C **86**, 064317 (2012).

[40] V. N. Kononov, B. D. Jurlov, E. D. Poletaev, V. M. Timokhov, and G. N. Manturov, Yad. Konstanty **22**, 29 (1977).

[41] A. R. DeL. Musgrove, B. J. Allen, J. W. Boldeman, and R. L. Macklin, *Proceedings of the International Conference on Neutron Physics and Nuclear Data for Reactors and Other Applied Purposes* (Harwell, United Kingdom, 1978), p. 449.

[42] K. Wisshak, F. Voss, F. Käppeler, L. Kazakov, and G. Reffo, Phys. Rev. C **57**, 391 (1998).

[43] K. Wisshak, F. Voss, and F. Käppeler, Phys. Rev. C **57**, 3452 (1998).

[44] Y. Nakajima, A. Asami, Y. Kawarasaki, and Y. Furuta, *Proc. International Conference on Neutron Physics and Nuclear Data for Reactors and Other Applied Purposes* (Harwell, United Kingdom, 1978), p. 438.

[45] M. V. Bokhovko, L. E. Kazakov, V. N. Kononov, E. D. Poletaev, V. M. Timokhov, and A. A. Voevodskiy, Vopr. At. Nauki Tekh., Ser.: Yad. Konstanty **1985**, 12 (1985).

[46] T. Veerapaspong, M. Igashira, S. Mizuno, J.-I. Hori, and T. Ohsaki, J. Nucl. Sci. Technol. **36**, 855 (1999).

[47] R. W. Hockenbury, W. R. Koste, and R. A. Shaw, Bull. Am. Phys. Soc. **20**, 560 (1975).

[48] Yu. N. Trofimov, Vopr. At. Nauki Tekh., Ser.: Yad. Konstanty **1993**, 17 (1993).

[49] A. E. Johnsrud, M. G. Silbert, and H. H. Barschall, Phys. Rev. **116**, 927 (1959).

[50] M. Afzal Ansari, R. K. Y. Singh, R. P. Gautam, and S. Kailas, Ann. Nucl. Energy **26**, 553 (1999).

[51] C. Massimi *et al.*, Eur. Phys. J. A **50**, 124 (2014).

[52] M. B. Chadwick *et al.*, Nucl. Data Sheets **112**, 2887 (2011).

[53] Evaluated Nuclear Data Files, 2011, http://www-nds.iaea.org/exfor.htm

[54] K. Shibata *et al.*, J. Nucl. Sci. Technol. **48**, 1 (2011).

[55] Z. Bao, H. Beer, F. Käppeler, F. Voss, K. Wisshak, and T. Rauscher, At. Data Nucl. Data Tables **76**, 70 (2000).

[56] I. Dillmann, M. Heil, F. Käppeler, R. Plag, T. Rauscher, and F.-K. Thielemann, AIP Conf. Proc. **819**, 123 (2006).

[57] P. W. Merrill, Astrophys. J. **116**, 21 (1952).

[58] M. Busso, R. Gallino, and G. J. Wasserburg, Annu. Rev. Astron. Astrophys **37**, 239 (1999).

[59] F. Herwig, T. Blöcker, D. Schönberner, and M. El Eid, Astron. Astrohys. **324**, L81 (1997).

[60] N. Langer, A. Heger, S. Wellstein, and F. Herwig, Astron. Astrohys. **346**, L37 (1999).

[61] S. Goriely and N. Mowlavi, Astron. Astrohys. **362**, 599 (2000).

[62] S. Goriely and L. Siess, Astron. Astrohys. **421**, L25 (2004).

[63] S. Goriely and L. Siess, in *Proceedings of IAU Symposium No. 228*, edited by V. Hill, P. François, and F. Primas (Cambridge University Press, Cambridge, England, 2005), p. 451.

[64] F. Käppeler, K. A. Toukan, M. Schumann, and A. Mengoni, Phys. Rev. C **53**, 1397 (1996).

[65] L. Siess and M. Arnould, Astron. Astrophys. **489**, 395 (2008).

PHYSICAL REVIEW C **92**, 064323 (2015)

# Photodisintegration of $^9$Be through the $1/2^+$ state and cluster dipole resonance

H. Utsunomiya,[1,2] S. Katayama,[1] I. Gheorghe,[3,4] S. Imai,[1] H. Yamaguchi,[2] D. Kahl,[2] Y. Sakaguchi,[2]
T. Shima,[5] K. Takahisa,[5] and S. Miyamoto[6]
[1]*Department of Physics, Konan University, Okamoto 8-9-1, Higashinada, Kobe 658-8501, Japan*
[2]*Center for Nuclear Study, University of Tokyo, Hirosawa 2-1, Wako, Saitama 351-0198, Japan*
[3]*ELI-NP, "Horia Hulubei" National Institute for Physics and Nuclear Engineering (IFIN-HH), 30 Reactorului,*
*077125 Bucharest-Magurele, Romania*
[4]*Faculty of Physics, University of Bucharest, RO-077125 Bucharest, Romania*
[5]*Research Center for Nuclear Physics, Osaka University, Suita, Osaka 567-0047, Japan*
[6]*Laboratory of Advanced Science and Technology for Industry, University of Hyogo, 3-1-2 Kouto, Kamigori, Ako-gun, Hyogo 678-1205, Japan*
(Received 5 November 2015; published 29 December 2015)

Photodisintegration of $^9$Be through the $1/2^+$ state near neutron threshold and cluster dipole resonance below giant dipole resonance was measured with quasi-monochromatic $\gamma$-ray beams produced in the inverse Compton scattering of laser photons. The cross section for the $1/2^+$ state is revisited, being consistent with the 2001 data. The cross section for the cluster dipole resonance is consistent with the cluster dipole sum-rule which however degenerates for the two-body ($n$-$^8$Be) and three-body($n$-$\alpha$-$\alpha$) configurations.

DOI: 10.1103/PhysRevC.92.064323 PACS number(s): 25.20.Lj, 24.30.Gd, 27.20.+n

## I. INTRODUCTION

Photodisintegration of $^9$Be has drawn a renewed attention from the viewpoints of explosive nucleosynthesis of $^9$Be and nuclear structure of the Borromean system. The nucleosynthesis of $^9$Be may proceed through $\alpha + \alpha \rightleftharpoons {}^8$Be and $^8$Be$(n,\gamma)^9$Be reaction [1] in astrophysical sites like Type-II supernovae [2] or neutron star mergers [3]. The explosive synthesis of $^9$Be followed by $^9$Be$(\alpha,n)^{12}$C may dominate over the triple $\alpha$ reaction to bridge the mass gaps at $A = 5$ and $A = 8$ [4]. Obviously, the $^8$Be$(n,\gamma)^9$Be reaction cannot be investigated in the experimental laboratory because $^8$Be is unstable. In contrast, the inverse photodisintegration of $^9$Be is experimentally feasible and straightforward. Previously two experiments were performed to measure the photodisintegration cross section using quasi-monochromatic $\gamma$-ray beams produced in the inverse Compton scattering of laser photons with relativistic electrons [5,6]. The discrepancy between the two measurements is significant for the $1/2^+$ state near the $n$-$^8$Be threshold.

The big-bang nucleosynthesis of $^9$Be may be catalyzed by a hypothetical long-lived negatively charged massive ($\gtrsim$100 GeV) leptonic particle, $X^-$, through the two-step resonant reaction $(^8\mathrm{Be}X^-)_{\mathrm{atom}} + n \to (^9\mathrm{Be}_{\frac{1}{2}^+}X^-)_{\mathrm{atom}} \to {}^9\mathrm{Be}_{\frac{3}{2}^-} + X^-$ [7]. A candidate for $X^-$ is the supersymmetric (SUSY) counterpart of the tau lepton ($\tau$), i.e., the stau ($\tilde{\tau}$) [8]. The observational upper limit in old stars, $^9\mathrm{Be}/\mathrm{H} \leqslant 2.1 \times 10^{-13}$, may impose a strong constraint on the lifetime of $X^-$. It is however pointed out [9] that accurate information of the excitation energy of $^9\mathrm{Be}_{\frac{1}{2}}^+$ as well as the charge radius of $^8$Be is required to calculate the reaction rate that is strongly affected by the resonance position of $(^9\mathrm{Be}_{\frac{1}{2}^+}X^-)_{\mathrm{atom}}$ with respect to the $(^8\mathrm{Be}X^-)_{\mathrm{atom}} + n$ threshold.

Besides its astrophysical significance, the $1/2^+$ state has raised an important question about the nuclear structure of $^9$Be in terms of resonant state [10–12] or virtual [13–15] state. The threshold behavior of the $1/2^+$ state cross section may be attributed to a virtual state that is defined as a pole of the $n$-$^8$Be scattering matrix at the complex wave number $k = -i\kappa$ ($\kappa > 0$) as well as a resonant state at $k = k_1 - ik_2$ ($k_1 > k_2 > 0$).

An enhancement in photoneutron emission was reported for $^9$Be in the energy region of 5–17 MeV immediately below the giant-dipole resonance (GDR) in the experiment with bremsstrahlung [16]. We hereby refer to the enhanced cross section as cluster dipole resonance (CDR) as we discuss in terms of the cluster dipole sum rule in Sec. IV. An experimental confirmation of the cross section is desirable to investigate the nuclear structure of CDR in the Borromean nucleus with a weakly bound neutron.

In this paper, we present experimental data for photodisintegration of $^9$Be through the $1/2^+$ state and CDR.

## II. EXPERIMENTAL PROCEDURE

We investigated photodisintegration of $^9$Be through the $1/2^+$ state and CDR at the NewSUBARU synchrotron radiation facility. Quasi-monochromatic $\gamma$-ray beams were produced by the Compton backscattering between laser photons with 100% linear polarization and relativistic electrons in a head-on collision geometry [17]. The laser Compton scattering (LCS) $\gamma$-ray beam produced in the head-on collision is also linearly polarized nearly 100%. We present here details of the experiment with emphasis on the characteristics of the LCS $\gamma$-ray beam and the neutron detection.

### A. Gamma beam production and energy profile

The $\gamma$-ray production beam line BL01 is shown in Fig. 1. Low- and high-energy $\gamma$-ray beams were produced using a grating-fixed CW CO$_2$ laser ($\lambda = 10.5915\,\mu$m $\pm 3\,$Å and a Q-switch Nd:YVO$_4$ INAZUMA laser ($\lambda = 1064$ nm), respectively. The nominal value of the electron beam energy was changed from 974 to 954 MeV in the decelerate mode of the storage ring and from 974 to 1121 MeV in the acceleration mode for low-energy $\gamma$ production, while it was changed from

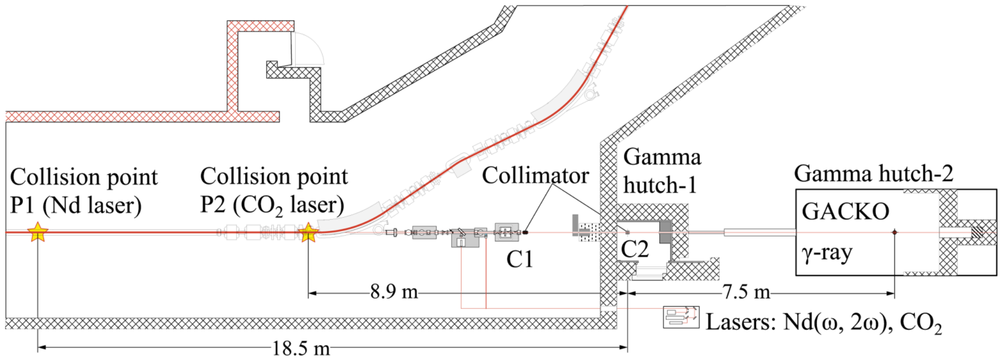

FIG. 1. (Color online) The $\gamma$-ray production beam line at the NewSUBARU synchrotron radiation facility.

974 to 962 MeV for the high-energy $\gamma$ production. The beam line has two collision points, P1 for the Nd:$YVO_4$ laser and P2 for the $CO_2$ laser, located at 18.5 m and 8.9 m from a collimator C2 mounted in the Hutch 1. We used a 1 mm-diameter C2 collimator to produce low-energy $\gamma$-ray beams and a 2 mm-diameter C2 collimator to produce high-energy beams. In addition to the C2 collimator, a 3 mm-diameter C1 collimator was mounted in the storage-ring vault. All collimators are made of 10 cm-thick Pb.

Low-energy LCS $\gamma$-ray beams were measured with a high-purity Ge detector to determine the energy profile of the $\gamma$-ray beam, while high-energy $\gamma$-ray beams with a 3.5 in. × 4.0 in. $LaBr_3$(Ce) detector. The Ge crystal of 64.3 mm diameter and 60.1 mm length was irradiated 15 mm off the center to avoid the central hole for the inner electrode and cooling rod.

Figure 2 shows an example of response function of the Ge detector to a low-energy LCS $\gamma$-ray beam. The Ge detector was calibrated with the standard $\gamma$-ray sources ( $^{133}$Ba, $^{137}$Cs, and $^{60}$Co including the sum peak). The full-energy peak is characterized by a high-energy edge and a low-energy tail. The edge slightly slopes, reflecting the energy resolutions of the electron beam ($\sim 4 \times 10^{-4}$) and the Ge detector. The energy spread of the tail reflects the kinematics of the Compton backscattering between laser photons and relativistic electrons into an aperture of the collimator. Monte Carlo simulations with the GEANT4 code [18] were carried out to reproduce the response function. The electron beam emittance, the double collimators, and the off-center irradiation of the Ge crystal were incorporated into the simulation. The response function (solid line) was well reproduced by the simulation (dotted line). By turning off the interaction of $\gamma$ rays with the detector material (Ge) in the simulation code, we obtained an energy spectrum of the LCS $\gamma$-ray beam produced. The spectrum is shown by the grey line in Fig. 2. The energy spread of the low-energy $\gamma$-ray beams used for the study of the $1/2^+$ state was 1.8–3.5% in full width at half-maximum (FWHM).

Figure 3 shows an example of response function of the $LaBr_3$(Ce) detector to a high-energy LCS $\gamma$-ray beam. The energy calibration of the high-energy LCS $\gamma$-ray beams relied on the absolute calibration of the electron beam energies with the accuracy on the order of $10^{-5}$ [19]. The full-energy peak is visible for the 5.5 MeV $\gamma$-ray beam. Again the response function was well reproduced by the simulation. The energy spread of the high-energy $\gamma$-ray beams used for the study of the CDR was 1.4–2.2% in FWHM.

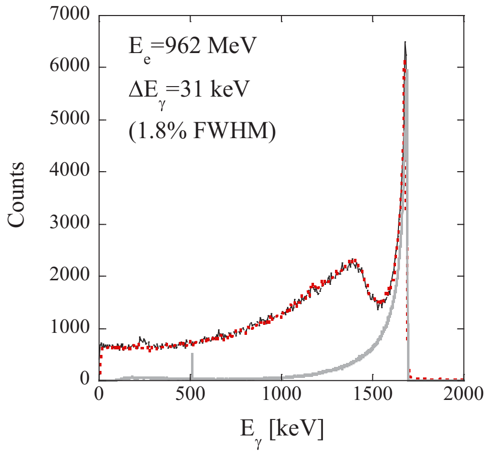

FIG. 2. (Color online) An experimental response function (solid line) of the Ge detector to a low-energy LCS $\gamma$-ray beam produced with the $CO_2$ laser along with the simulated response function (dotted line) and energy distribution of the LCS $\gamma$-ray beam (grey line).

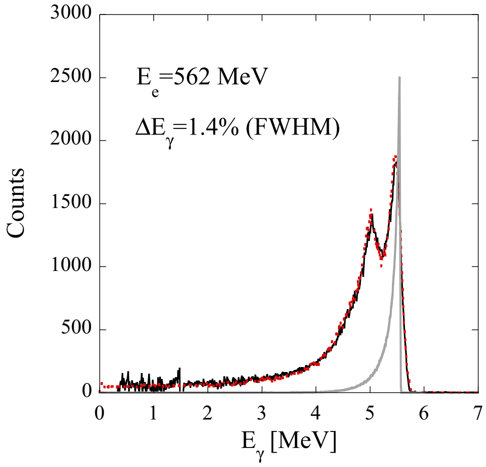

FIG. 3. (Color online) An experimental response function (solid line) of the $LaBr_3$(Ce) detector to a high-energy LCS $\gamma$-ray beam produced with the Nd:$YVO_4$ laser along with the simulated response function (dotted line) and energy distribution of the LCS $\gamma$-ray beam (grey line).

The intensity distribution of the LCS $\gamma$-ray beam at the target position was simulated with the GEANT4 code. With the 2 mm C2 collimator, the beam size on target was 2.3 mm in diameter in FWHM of the intensity distribution.

### B. Target

A 99% $^9$Be rod of 25 mm diameter and 40 mm length was used as a target. A natural carbon rod of the same dimension was also used to investigate the scattering effect of the LCS $\gamma$-ray beam [6]. No scattering effects were found compared with blank target runs. Heavy water (99.9%) in an aluminum container with entrance and exit windows of 25.4 $\mu$m-thick Kapton foil was used as a $D_2O$ target of 14 mm diameter and 100 mm length. Photodisintegration of deuterium was measured at the electron beam energy 1460 MeV for a crosscheck of the present absolute cross section measurement. An empty target run confirmed a negligible effect of the Kapton foils on photoneutron emission.

### C. $\gamma$-ray flux

A 8 in. × 12 in. NaI(Tl) detector with 100% detection efficiency was used as a $\gamma$-ray flux monitor. The flux determination is straightforward for LCS $\gamma$-ray beams produced with the CW $CO_2$ laser. The $\gamma$ rays were detected with the NaI(Tl) detector at the count rate of 15–41 kcps. Energy spectra were recorded with a multichannel analyzer with a conversion time of $\sim$2.6 $\mu$s. The flux was determined by subtracting background $\gamma$ rays and correcting for a small amount of double photon events.

The flux determination for pulsed LCS $\gamma$-ray beams produced with the Q-switch Nd:$YVO_4$ laser followed the Poisson-fitting method [20,21]. The laser was operated at 20 kHz. Laser photons with a pulse width 60 ns collide with relativistic electrons in the NewSUBARU storage ring at 500 MHz with a 20 ps pulse width. Although the number of pairs of laser photons and electrons involved in the collision during the 60 ns laser pulse ($N$) is large, the collision probability per photon-electron pair ($p$) is small. As a result, the number of collisions ($n$) is small with the average number $m = pN$. Under this condition, the distribution of the number of collision, $P_m(n)$, can be expressed by the Poisson distribution, $P_m(n) = \frac{m^n}{n} e^{-m}$. Multiphoton spectra generated by pulsed $\gamma$-ray beams measured with a NaI(Tl) were investigated at different $\gamma$-ray beam intensities and indeed characterized by the Poisson distribution [22]. Figure 4 shows a typical single- and multiphoton spectra. The number of $\gamma$ rays ($N_\gamma$) is determined by $N_\gamma = mN_p$ with the average number of $\gamma$ rays per $\gamma$ pulse and the number of $\gamma$ pulses, $N_p$. The $N_p$ is equal to the number of total events of the multiphoton spectrum which is often referred to as pile-up spectrum. Empirically, the average number of $\gamma$ rays per pulse $m$ is given by the ratio of the average channel number of the multiphoton spectrum $[CH]_p^{av}$ to that of the single-photon spectrum $[CH]_s^{av}$, $m = \frac{[CH]_p^{av}}{[CH]_s^{av}}$ [22]. The uncertainty of the flux determination comes from the energy linearity in the response of the flux monitor detector to multiphotons. The uncertainty was estimated to be $\sim$3% [22].

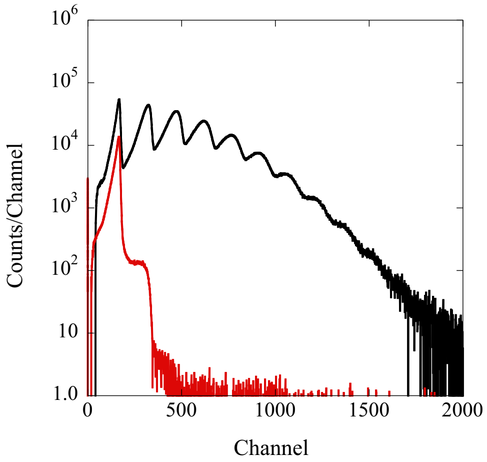

FIG. 4. (Color online) Multiphoton and single-photon spectra of the LCS $\gamma$-ray beam measured with the NaI(Tl) detector.

### D. Neutron detection

Photoneutrons were detected with a 4$\pi$ neutron detector composed of 20 $^3$He proportional counters embedded in a polyethylene moderator in a triple-ring configuration. The concentric Ring-1 (R1), Ring-2 (R2), and Ring-3 (R3) of four, eight, and eight $^3$He counters are placed at the distances of 38, 70, and 100 mm from the beam axis, respectively. This detector is designed with the MCNP code [23] for a highest total efficiency being more than 60% for neutrons below 1 MeV. Figure 5 shows detection efficiencies of Ring-1, Ring-2, and Ring-3 as well as the sum efficiency for isotropically emitted neutrons. The efficiencies were calibrated with a $^{252}$Cf source at the National Metrology Institute of Japan (NMIJ). The detector has long been used for ($\gamma$, $n$) cross section measurements for heavy nuclei (see [24,25]

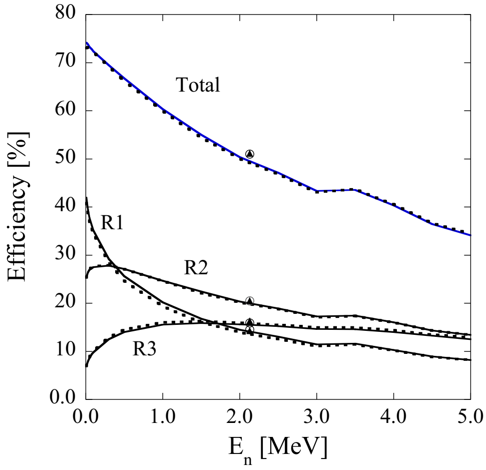

FIG. 5. (Color online) The detection efficiencies of the Ring-1, Ring-2, and Ring-3 and the total efficiency for $s$-wave (solid line) and $p$-wave (dotted lines) neutrons obtain by the GEANT4 simulation. The efficiencies measured with a calibrated $^{252}$Cf source are shown by the solid triangles and those simulated with the MCNP Monte Carlo code are shown by the open circles.

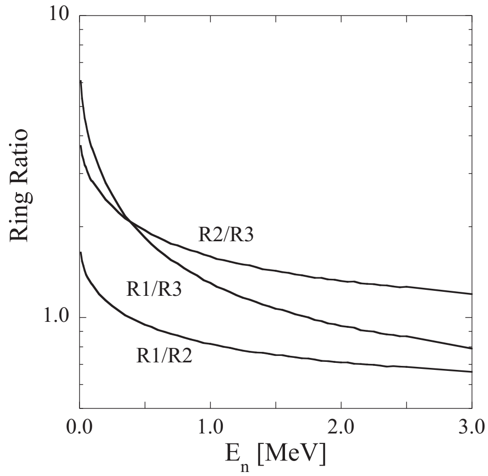

FIG. 6. The ring ratios of the present $4\pi$ neutron detector with Ring-1, Ring-2, and Ring-3 of four, eight, and eight $^3$He counters embedded in a polyethylene moderator.

for the latest measurements and references therein). The detection efficiencies were recalibrated in advance to the present experiment using a $^{252}$Cf source at a neutron emission rate $2.27 \times 10^4$ s$^{-1}$ with 2.2% uncertainty at the NMIJ. The experimental calibration points were excellently reproduced.

There are two dominating modes of $s$-wave and $p$-wave photoneutron emissions. Besides the isotropic emission of $s$-wave neutrons, the detection efficiencies were also simulated for $p$-wave neutrons with the angular distribution $W_{\mathrm{pol}}(\theta,\phi) = \frac{3}{8\pi}[\sin^2\theta(1+\cos 2\phi)]$, where $\theta$ stands for the polar angle for photoneutron emission with respect to the beam direction ($z$ axis), while $\phi$ for the azimuthal angle with respect to the linear polarization ($x$ axis) of the $\gamma$-ray beam defined by a direction of the electric field. The results are shown in Fig. 5. One can see that Ring-1, Ring-2, and Ring-3 summed over four, eight, and eight $^3$He counters, respectively, have the same efficiencies as for $s$- and $p$-wave neutrons. The angular distribution of p-wave neutrons is largely smeared out in the polyethylene moderator.

Figure 6 shows ratios of the detection efficiencies of Ring-1, Ring-2, and Ring-3 as a function of the neutron energy. The ring-ratio technique [26] which takes advantage of these unique energy dependences was used to determine the mean energy of neutrons emitted in each $\gamma$-ray beam irradiation; the neutron energies determined with the three ring ratios were weight-averaged. The weighted average was in turn used to determine the total detection efficiency of the $4\pi$ neutron detector. The mean neutron energy changed from 16 keV to 200 keV in the photodisintegration of $^9$Be through the $1/2^+$ state, while it changed from 1.15 MeV to 1.99 MeV in the photodisintegration through CDR.

## III. DATA REDUCTION

The experimental formula of photoneutron cross section is given by

$$\int_{S_n}^{E_{\max}} n_\gamma(E_\gamma)\sigma(E_\gamma)dE_\gamma = \frac{N_n}{N_t N_\gamma \xi \epsilon_n g}, \qquad (1)$$

where $S_n$ is the neutron threshold energy, $E_{\max}$ is the maximum energy of the LCS $\gamma$-ray beam, $n_\gamma(E_\gamma)$ gives the energy distribution of the $\gamma$-ray beam normalized to unity and $\sigma(E_\gamma)$ is the photoneutron cross section to be determined. Furthermore, $N_n$ represents the number of neutrons detected, $N_t$ gives the number of target nuclei per unit area, $N_\gamma$ is the number of $\gamma$ rays incident on target, $\epsilon_n$ represents the neutron detection efficiency, and finally $\xi = (1-e^{\mu t})/(\mu t)$ gives a correction factor for a thick target measurement. The factor $g$ represents a fraction of the $\gamma$ flux above $S_n$.

The monochromatic cross section results when the $n(E_\gamma)$ in Eq. (1) is replaced by a $\delta$ function, $\delta(E_\gamma - E_0)$:

$$\sigma^{\mathrm{mon}}(E_0) = \frac{N_n}{N_t N_\gamma \xi \epsilon_n g}. \qquad (2)$$

There are two methods for deconvoluting the integral of Eq. (1) to obtain $\sigma(E_\gamma)$, the Taylor expansion method [24] and the least-squares method [27]. We summarize the Taylor expansion method which has long been used in ($\gamma$, $n$) cross section measurements for heavy nuclei (see [24] and references therein).

A deconvolution can be done by expanding $\sigma(E_\gamma)$ in the Taylor series at the average energy $E_{\mathrm{av}}$:

$$\sigma(E_\gamma) = \frac{1}{n!}\sum_{n=0}^{\infty}\sigma^{(n)}(E_{\mathrm{av}})(E_\gamma - E_{\mathrm{av}})^n. \qquad (3)$$

Putting Eq. (3) into Eq. (1), one obtains

$$\sigma(E_{\mathrm{av}}) = \sigma^{\mathrm{mon}}(E_{\mathrm{av}}) - s_2(E_{\mathrm{av}}) - s_3(E_{\mathrm{av}}) - \cdots, \qquad (4)$$

where

$$s_n(E_{\mathrm{av}}) = \frac{1}{n!}\sigma^{(n)}(E_{\mathrm{av}})\int_{S_n}^{E_{\max}} n_\gamma(E_\gamma)(E_\gamma - E_{\mathrm{av}})^n dE_\gamma \qquad (5)$$

and

$$\sigma^{(n)}(E_{\mathrm{av}}) = \left.\frac{d^n\sigma(E)}{dE^n}\right|_{E=E_{\mathrm{av}}}. \qquad (6)$$

Note that $s_1$ is zero by the definition of $E_{\mathrm{av}}$.

Since $\sigma^{(i)}(E_{\mathrm{av}})$ cannot be calculated until $\sigma(E_\gamma)$ is determined, an iteration procedure must be employed. The iteration begins with a best fit to the monochromatic cross section with an appropriate function and ends with a reasonable conversion. In the present data reduction, we used the Breit-Wigner formula for the $1/2^+$ data and a Lorentzian function for a specific fit to the CDR data. We approximate the best-fit function with the third-order polynomial in small energy bins to terminate the Taylor expansion at $s_3$ in Eq. (4).

The systematic uncertainty is estimated to be 4.4% which is a quadratic sum of 3% for the number of incident photons and 3.2% for the neutron detection efficiency.

## IV. RESULTS AND DISCUSSIONS

### A. Crosscheck with the D($\gamma$,$n$)$p$ cross section

The result of the present measurement of the D($\gamma$,$n$)$p$ reaction cross section is shown in Fig. 7. The present result is in good agreement with the existing data [28–32] and the JENDL evaluation [33].

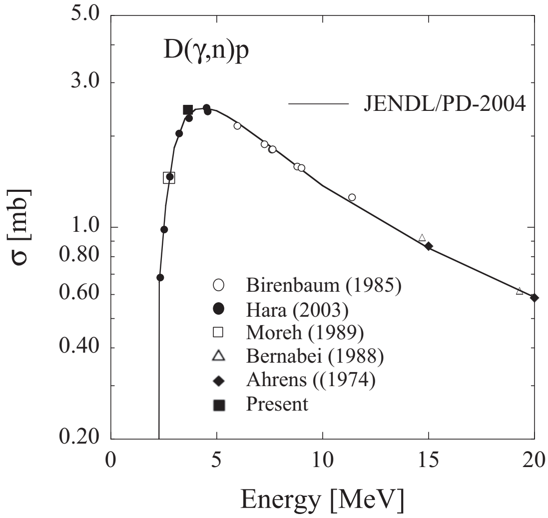

FIG. 7. The D($\gamma,n$) cross section. The present datum is shown by the solid square.

The same LCS $\gamma$-ray beam was also used to measure the photodisintegration cross section for $^9$Be. The result is shown by the thick open cross in Fig. 8 in comparison with the 2001 data (filled circles) [5] and 2012 data (open circles) [6]. The bremsstrahlung data (crosses) [16] are also shown in the figure. The 2012 data are the monochromatic cross sections retrieved from the EXFOR database [34]. We remark that the 2001 data were published in such a way that cross sections are plotted at the peak energies of the $\gamma$-ray beams with the horizontal error bars representing energy spreads of the beams in FWHM.

### B. 1/2$^+$ state

The mean neutron energy, $E_n^{\mathrm{av}}$, determined with the ring ratio technique is shown in Fig. 9 as a function of the $\gamma$-ray energy. The mean neutron energies near the $n$-$^8$Be threshold are consistent with the kinematics of two-body breakup $^9\mathrm{Be} \rightarrow n + {}^8\mathrm{Be}$, $E_n = \frac{8}{9}(E_\gamma - S_n)$. However, the $E_n^{\mathrm{av}}$ deviates from the two-body kinematics at the three energies above 1.8 MeV. The deviation indicates the onset of three-body breakup, $^9\mathrm{Be} \rightarrow n + \alpha + \alpha$, in this energy region.

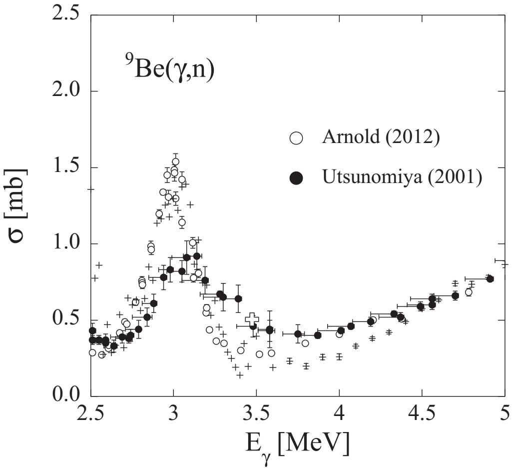

FIG. 8. The $^9$Be($\gamma,n$) cross section. The present datum is shown by the thick open cross.

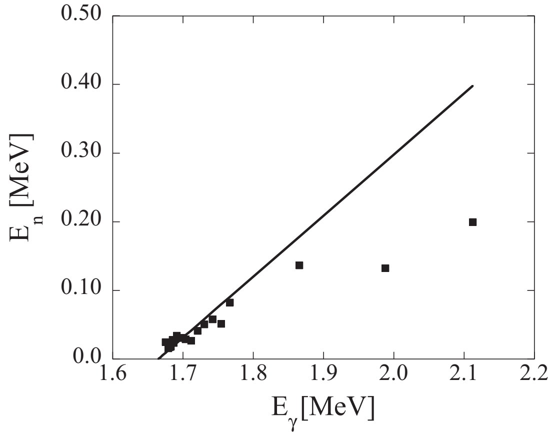

FIG. 9. The mean neutron kinetic energies determined by the ring ratio technique [26]. The two-body kinematics is shown by the solid line.

Figure 10 shows the present cross section for the 1/2$^+$ state by the solid squares. The data were corrected for energy spreads of the LCS $\gamma$-ray beam with the Taylor expansion method. The monochromatic cross section is also shown by the open circles in the figure. The present measurement between the $n$-$^8$Be threshold at 1.665 MeV and the $n$-$\alpha$-$\alpha$ threshold at 1.573 MeV provided a vanishing cross section ($9.3 \times 10^{-5} \pm 0.016$ mb) at 1.63 MeV.

The data measured from the $n$-$^8$Be threshold to 1.78 MeV were fitted with the Breit-Wigner (B-W) function with a focus on the low-energy behavior of the cross section:

$$\sigma(E_\gamma) = \pi\left(\frac{\hbar c}{E_\gamma}\right)^2 \frac{\Gamma_\gamma \Gamma_n}{(E_\gamma - E_R)^2 + (\Gamma/2)^2}. \qquad (7)$$

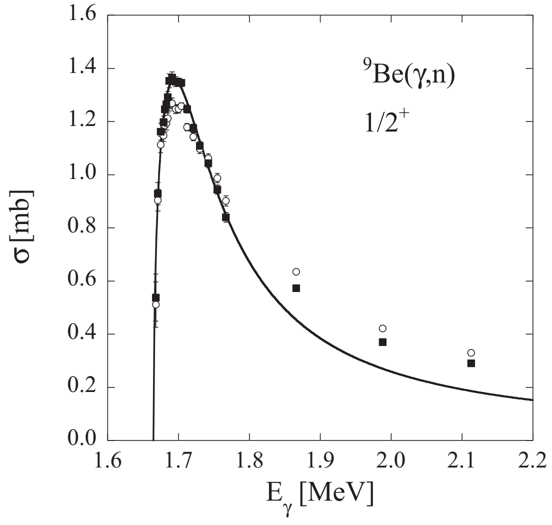

FIG. 10. The present $^9$Be($\gamma,n$) cross section corrected for the energy spread of the LCS $\gamma$-ray beam is shown by the solid squares and the monochromatic cross section is shown by the open circles. The solid line represents the Breit-Wigner fit to the cross section.

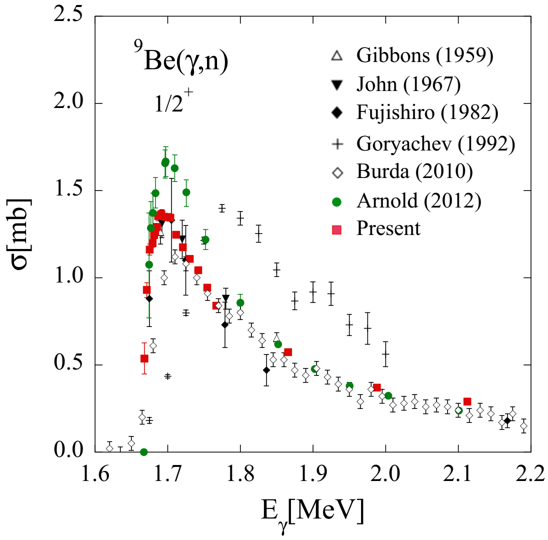

FIG. 11. (Color online) The present $^9$Be$(\gamma,n)$ cross section in comparison with the existing data (filled circles: Ref. [6], filled diamonds: Ref. [42], inverted filled triangles: Ref. [40], open triangles: Ref. [41], crosses: Ref. [16], open diamonds: Ref. [38]).

The $\gamma$ width $\Gamma_\gamma$ is related to the reduced transition probability $B(E1)\downarrow$ [35] by

$$\Gamma_\gamma = \frac{16\pi}{9}\alpha(\hbar c)^{-2}E_\gamma^3 B(E1)\downarrow. \tag{8}$$

The neutron width $\Gamma_n$ for $s$-wave neutrons from the $1/2^+$ state was taken [36] as

$$\Gamma_n = 2\sqrt{\epsilon_R(E_\gamma - S_n)}. \tag{9}$$

The threshold cross section is well fitted with the B-W function as shown by the solid line. The B-W fit, however, underestimates the experimental data measured above 1.8 MeV. This underestimate may be associated with the onset of the three-body breakup in this energy region as indicated by the mean neutron energies.

The best-fit resonance parameters are listed in Table I, in comparison with those of Refs. [5,6]. The present result is consistent with the 2001 data [5]. It is to be noted that the disagreement in $B(E1)$ between the $(\gamma,n)$ [5,37] and $(e,e')$ [38,39] data was recently analyzed and resolved as a way of integration of the resonance [12].

The threshold behavior of the present cross section is shown in Fig. 11 in comparison with the existing data including those taken with radioactive isotopes [40–42] and bremsstrahlung [16]. The deconvoluted cross section of the 2012 data (Fig. 7 of Ref. [6]) is shown in the figure. Note that the 2012 data give a peak cross section (∼1.7 mb) that is much higher than that (1.35 mb) of the present data. The data of the radioactive isotope measurements are rather consistent with the present data, while the bremsstrahlung data exhibit a very different threshold behavior. Averaged photoneutron cross sections extracted from the $(e,e')$ data [38,43] are also shown in the figure.

We remark that the B-W fit may not serve as evidence that the $1/2^+$ state is a resonant state though the energy and width parameters resulting from the $R$-matrix analysis are also consistent with the resonance nature of the $1/2^+$ state [12]. A similar threshold behavior of the cross section may arise from a virtual state in the potential model of $n$-$^8$Be scattering [13] and the complex scaling method of describing the $n$-$\alpha$-$\alpha$ system [15]. The authors were informed in private communication that the present cross section is reproduced by the complex scaling method [44].

### C. Cluster dipole resonance

A significant resonance was confirmed in the present measurement in the energy region immediately below GDR as shown in Fig. 12. The present data (filled squares) show even more enhanced cross sections than the bremsstrahlung data (crosses) at energies higher than 8 MeV. The cluster dipole resonance has a significant strength compared to the observed GDR. In the figure, the GDR data (open circles) are a sum of $(\gamma,n)$, $(\gamma,n+p)$, $(\gamma,2n)$, and $(\gamma,2n+p)$ cross sections of Ref. [45]. The 2001 data [5] (filled circles) are shown for the $5/2^+$ state. For the $1/2^+$ state, the present data as well as the deconvoluted cross section of Ref. [6] (filled diamonds) and the bremsstrahlung data of Ref. [16] (crosses) are shown.

The CDR strength was deduced by a global fit to the data of GDR [45], CDR, and the $5/2^+$ state [5] with the least-squares method. The Lorentzian and B-W functions were used for the GDR and the $5/2^+$ state, respectively, while the Gaussian function was used for CDR assuming that its strength is localized in the low-energy tail of the GDR. The best-fit function is shown by the dot-dashed line in Fig. 12 along with its breakdown to the GDR, CDR, and $5/2^+$ state by the dashed, solid, dotted lines, respectively. The energy-integrated strength of the CDR is 11.3 mb MeV.

We remark that the resonance strength depends on the shape of the low-energy tail of the GDR which is estimated by the Lorentzian function. The value (11.3 mb MeV) may represent a lower limit because it is known that the Lorentzian type of the $\gamma$-ray strength function (photoabsorption cross section) significantly overestimates $(n,\gamma)$ cross sections for

TABLE I. Resonance parameters obtained in the Breit-Wiger fit to the $(\gamma,n)$ cross section data for the $1/2^+$ state.

| $E_R$ (MeV) | $\Gamma_n$ (keV) | $\Gamma_\gamma$ (eV) | $B(E1)\downarrow$ ($e^2$ fm$^2$) | Ref. |
|---|---|---|---|---|
| 1.748 ± 0.01 | 283 ± 42 | 0.598 ± 0.004 | 0.107 ± 0.007 | Utsunomiya *et al.* [5] |
| 1.735 ± 0.003 | 225 ± 12 | 0.568 ± 0.001 | 0.104 ± 0.002 | Sumiyoshi *et al.* [37] |
| 1.731 ± 0.002 | 213 ± 6 | 0.738 ± 0.002 | 0.136 ± 0.002 | Arnold *et al.* [6] |
| 1.728 ± 0.001 | 214 ± 7 | 0.595 ± 0.002 | 0.111 ± 0.004 | Present |

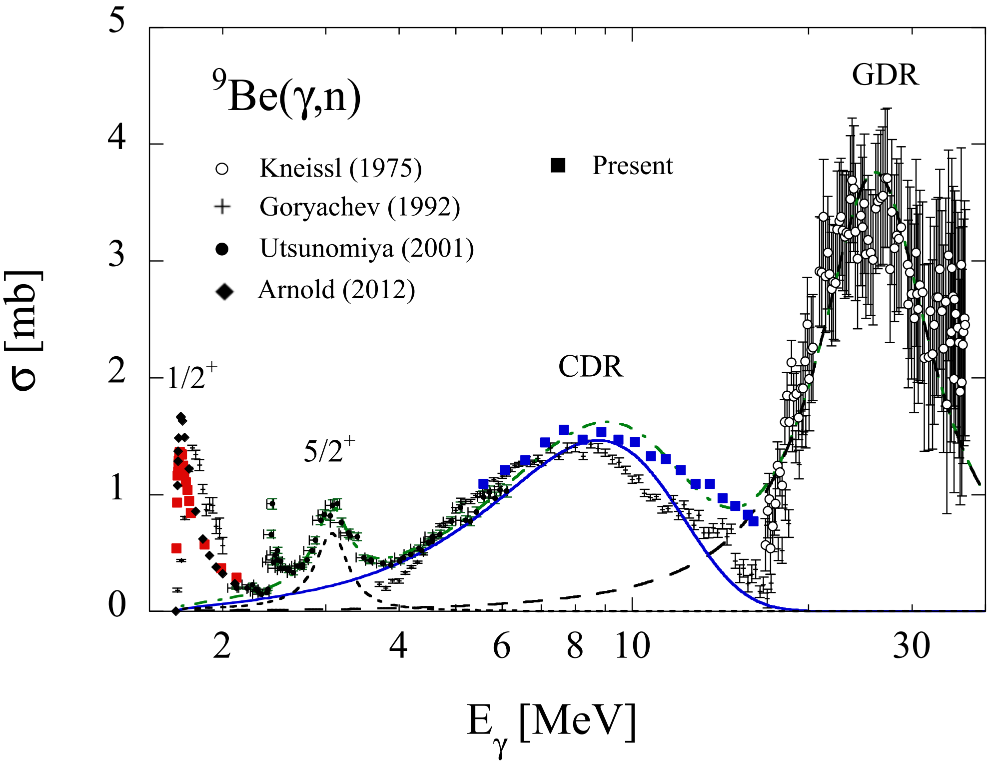

FIG. 12. (Color online) The $^9$Be($\gamma$,$n$) cross section in the energy region from the $n$ + $^8$Be threshold to GDR (see text for details).

heavy nuclei [46–49]. The strength integrated over 4–16 MeV without a contribution from the low-energy tail of the GDR is 14.2 mb MeV. Thus, the resonance strength is 11.3–14.2 mb MeV.

Let us compare the resonance strength with the cluster dipole sum rule [50–52] for the two-body ($n$-$^8$Be) and three-body ($n$-$\alpha$-$\alpha$) systems:

$$\int \sigma_{E1}(E)dE = 60\left(\frac{NZ}{A} - \sum_i \frac{N_iZ_i}{A_i}\right). \qquad (10)$$

The first term of Eq. (10) is the Thomas-Reiche-Kuhn (TRK) sum rule representing the $E1$ response of a nucleus in the absence of exchange forces. After subtracting the intrinsic contributions from the constituent clusters from the entire response, the sum rule represents the $E1$ response arising from relative motions between the constituents. The cluster dipole sum rule gives 10% (13.3 mb MeV) of the TRK sum rule (133 mb MeV), irrespective of the two-body ($n$-$^8$Be) or three-body ($n$-$\alpha$-$\alpha$) systems. The present strength is consistent with the cluster dipole sum rule, which however does not distinguish whether a neutron oscillates in the $n$-$^8$Be or $n$-$\alpha$-$\alpha$ configuration. It is desirable to investigate the nature of the cluster dipole resonance both experimentally and theoretically. The investigation requires a new experiment of $n$-$\alpha$-$\alpha$ coincidences to measure correlations of a neutron against two $\alpha$ particles. The authors are informed in private communication that a theoretical investigation is in progress based on the antisymmetrized molecular dynamics calculation [53].

## V. CONCLUSIONS

The photodisintegration of $^9$Be through the $1/2^+$ state and cluster dipole resonance was measured. The cross section of the $1/2^+$ state is consistent with the 2001 data and the data of the radioactive isotope measurements. The observed resonance strength is consistent with the cluster dipole sum rule. However, the sum rule degenerates in the two-body ($n$-$^8$Be) and three-body ($n$-$\alpha$-$\alpha$) systems. Consequently, the present result does not distinguish whether a neutron oscillates in the two-body or three-body configuration. A new $n$-$\alpha$-$\alpha$ coincidence experiment is needed to investigate the configuration. A theoretical study is encouraged to investigate the nature of the $1/2^+$ state and the nuclear structure of the cluster dipole resonance in $^9$Be.

## ACKNOWLEDGMENTS

We are indebted to Masayasu Kamimura of RIKEN for drawing our attention to the stau-catalyzed big-bang nucleosynthesis and Kiyoshi Kato of Hokkaido University for discussions on resonant and virtual states. We thank Akinori Takemoto and Masashi Yamaguchi for their assistance in tuning the $CO_2$ laser and the double collimators for producing low-energy LCS $\gamma$-ray beams. This work was supported by the Japan Private School Promotion Foundation. I.G. acknowledges financial support from the Extreme Light Infrastructure Nuclear Physics (ELI-NP) Phase I, a project cofinanced by the Romanian Government and the European Union through the European Regional Development Fund (425/12.12.2012, POS CCE, ID 1334 SMIS-CSNR 40741).

[1] T. Sasaqui, K. T. Kajino, G. Mathews, K. Otsuki, and T. Nakamura, Astrophys. J. **634**, 1173 (2005).

[2] S. E. Woosley, J. R. Wilson, G. J. Mathews, R. D. Hoffmman, and B. S. Meyer, Astrophys. J. **433**, 229 (1994).

[3] C. Freburghaus, S. Rosswog, and F.-K. Thielemann, Astrophys. J. **525**, L121 (1999).

[4] M. Terasawa, K. Sumiyoahi, T. Kajino, G. Mathews, and I. Tanihata, Astrophys. J. **562**, 470 (2001).

[5] H. Utsunomiya, Y. Yonezawa, H. Akimune, T. Yamagata, M. Ohta, M. Fujishiro, H. Toyokawa, and H. Ohgaki, Phys. Rev. C **63**, 018801 (2000).

[6] C. W. Arnold, T. B. Clegg, C. Iliadis, H. J. Karwowski, G. C. Rich, J. R. Tompkins, and C. R. Howell, Phys. Rev. C **85**, 044605 (2012).

[7] M. Pospelov, J. Pradler, and F. D. Steffen, J. Cosmol. Astropart. Phys. **11**, 020 (2008).

[8] F. Iocco, G. Mangano, G. Miele, O. Pisanti, and P. D. Serpico, Phys. Rep. **472**, 1 (2009).

[9] M. Kamimura, Y. Kino, and E. Hiyama, Prog. Theor. Phys. **121**, 1059 (2009).

[10] E. Garrido, D. V. Fedorov, and A. S. Jense, Phys. Lett. B **684**, 132 (2010).

[11] R. Álvarez-Rodríguez, A. S. Jensen, E. Garrido, and D. V. Fedorov, Phys. Rev. C **82**, 034001 (2010).

[12] V. D. Efros, P. von Neumann-Cosel, and A. Richter, Phys. Rev. C **89**, 027301 (2014).

[13] V. D. Efros and J. M. Bang, Eur. Phys. J. A **4**, 33 (1999).

[14] K. Arai, P. Descouvemont, D. Baye, and W. N. Catford, Phys. Rev. C **68**, 014310 (2003).

[15] M. Odsuren, Y. Kikuchi, T. Myo, M. Aikawa, and K. Kato, Phys. Rev. C **92**, 014322 (2015).

[16] A. M. Goryachev, G. N. Zalesnyy, and I. V. Pozdnev, Izv. Ross. Akad. Nauk, Ser. Fiz. **56**, 159 (1992).

[17] S. Amano, K. Horikawa, K. Ishihara, S. Miyamoto, T. Hayakawa, T. Shizuma, and T. Mochizuki, Nucl. Instrum. Methods Phys. Res. A **602**, 337 (2009).

[18] S. Agostinelli *et al.*, Nucl. Instrum. Methods Phys. Res. A **506**, 250 (2003).

[19] H. Utsunomiya *et al.*, IEEE Trans. Nucl. Sci. **61**, 1252 (2014).

[20] T. Kii *et al.*, in *Proceedings of the 12th Symposium on Accelerator Science and Technology*, edited by Yasushige Yano (The Institute of Physical and Chemical Research (RIKEN), Wako, Japan, 1999), pp. 484–485.

[21] H. Toyokawa, T. Kii, H. Ohgaki, T. Shima, T. Baba, and Y. Nagai, IEEE Trans. Nucl. Sci. **47**, 1954 (2000).

[22] T. Kondo *et al.*, Nucl. Instrum. Methods Phy. Res. A **659**, 462 (2011).

[23] J. F. Briesmeister, computer code MCNP, Version 4C (Los Alamos National Laboratory, Los Alamos, 2000).

[24] D. M. Filipescu, I. Gheorghe, H. Utsunomiya, S. Goriely, T. Renstrom, H. T. Nyhus, O. Tesileanu, T. Glodariu, T. Shima, K. Takahisa, S. Miyamoto, Y. W. Lui, S. Hilaire, S. Peru, M. Martini, and A. J. Koning, Phys. Rev. C **90**, 064616 (2014).

[25] H. T. Nyhus, T. Renstrom, H. Utsunomiya, S. Goriely, D. M. Filipescu, I. Gheorghe, O. Tesileanu, T. Glodariu, T. Shima, K. Takahisa, S. Miyamoto, Y. W. Lui, S. Hilaire, S. Peru, M. Martini, L. Siess, and A. J. Koning, Phys. Rev. C **91**, 015808 (2015).

[26] B. L. Berman, R. E. Pywell, S. S. Dietrich, M. N. Thompson, K. G. McNeill, and J. W. Jury, Phys. Rev. C **36**, 1286 (1987).

[27] O. Itoh *et al.*, J. Nucl. Sci. Technol. **48**, 834 (2011).

[28] J. Ahrens *et al.*, Phys. Lett. B **52**, 49 (1974).

[29] Y. Birenbaum, S. Kahane, and R. Moreh, Phys. Rev. C **32**, 1825 (1985).

[30] R. Bernabei, A. Chisholm, S. dAngelo, M. P. DePascale, P. Picozza, C. Schaerf, P. Belli, L. Casano, A. Incicchitti, D. Prosperi, and B. Girolami, Phys. Rev. C **38**, 1990 (1988).

[31] R. Moreh, T. J. Kennett, and W. V. Prestwich, Phys. Rev. C **39**, 1247 (1989).

[32] K. Y. Hara, H. Utsunomiya, S. Goko, H. Akimune, T. Yamagata, M. Ohta, H. Toyokawa, K. Kudo, A. Uritani, Y. Shibata, Y. W. Lui, and H. Ohgaki, Phys. Rev. D **68**, 072001 (2003).

[33] http://wwwndc.jaea.go.jp/jendl/j40/J40_J.html.

[34] https://www-nds.iaea.org/exfor/exfor.htm.

[35] J. M. Blatt and V. F. Weisskopf, *Theoretical Nuclear Physics* (Springer-Verlag, New York, 1952), p. 583.

[36] E. Wigner, Phys. Rev. **73**, 1002 (1948).

[37] K. Sumiyoshi, H. Utsunomiya, S. Goko, and T. Kajino, Nucl. Phys. A **709**, 467 (2002).

[38] O. Burda, P. von Neumann-Cosel, A. Richter, C. Forssén, and B. A. Brown, Phys. Rev. C **82**, 015808 (2010).

[39] J. P. Glickman, W. Bertozzi, T. N. Buti, S. Dixit, F. W. Hersman, C. E. Hyde-Wright, M. V. Hynes, R. W. Lourie, B. E. Norum, J. J. Kelly, B. L. Berman, and D. J. Millener, Phys. Rev. C **43**, 1740 (1991).

[40] J. H. Gibbons *et al.*, Phys. Rev. **114**, 1319 (1959).

[41] W. John and J. M. Prosser, Phys. Rev. **163**, 958 (1967).

[42] M. Fujishiro *et al.*, Can. J. Phys. **60**, 1672 (1982); **61**, 1579 (1983).

[43] G. Kuechler, A. Richter, and W. von Witsch, Z. Phys. A **326**, 447 (1987).

[44] Y. Kikuchi (private communication).

[45] U. Kneissl, G. Kuhl, K.-H. Leister, and A. Weller, Nucl. Phys. A **247**, 91 (1975).

[46] H. Utsunomiya, S. Goriely, M. Kamata, T. Kondo, O. Itoh, H. Akimune, T. Yamagata, H. Toyokawa, Y. W. Lui, S. Hilaire, and A. J. Koning, Phys. Rev. C **80**, 055806 (2009).

[47] H. Utsunomiya, S. Goriely, H. Akimune, H. Harada, F. Kitatani, S. Goko, H. Toyokawa, K. Yamada, T. Kondo, O. Itoh, M. Kamata, T. Yamagata, Y. W. Lui, S. Hilaire, and A. J. Koning, Phys. Rev. C **81**, 035801 (2010).

[48] H. Utsunomiya, S. Goriely, H. Akimune, H. Harada, F. Kitatani, S. Goko, H. Toyokawa, K. Yamada, T. Kondo, O. Itoh, M. Kamata, T. Yamagata, Y. W. Lui, I. Daoutidis, D. P. Arteaga, S. Hilaire, and A. J. Koning, Phys. Rev. C **82**, 064610 (2010).

[49] H. Utsunomiya, S. Goriely, M. Kamata, H. Akimune, T. Kondo, O. Itoh, C. Iwamoto, T. Yamagata, H. Toyokawa, Y. W. Lui, H. Harada, F. Kitatani, S. Goko, S. Hilaire, and A. J. Koning, Phys. Rev. C **84**, 055805 (2011).

[50] Y. Alhassid, M. Gai, and G. F. Bertsch, Phys. Rev. Lett. **49**, 1482 (1982).

[51] H. Sagawa and M. Honma, Phys. Lett. B **251**, 17 (1990).

[52] R. deDiego, E. Garrido, A. S. Jensen, and D. V. Fedorov, Phys. Rev. C **77**, 024001 (2008).

[53] Y. Kanada-En'yo (private communication).